Neuron

Article

Molecular logic of synaptic diversity between *Drosophila* tonic and phasic motoneurons

Graphical abstract

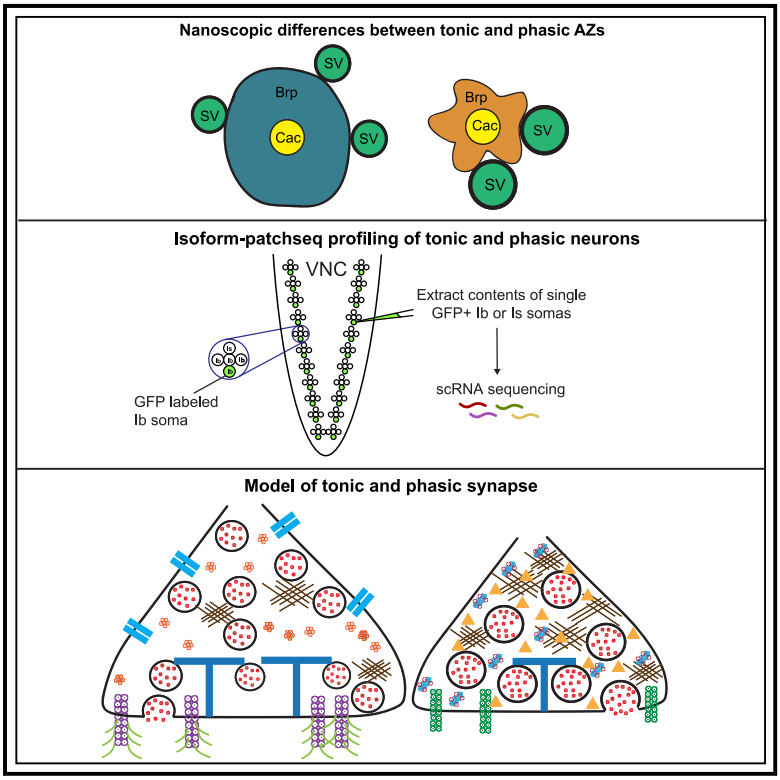

Authors

Suresh K. Jetti, Andrés B. Crane, Yulia Akbergenova, Nicole A. Aponte-Santiago, Karen L. Cunningham, Charles A. Whittaker, J. Troy Littleton

Correspondence

sureshj@mit.edu S.K.J.), troy@mit.edu J.T.L.)

In brief

Jetti et al. describe nanoscopic and transcriptomic correlates that underlie differences in diverse synaptic properties of *Drosophila* tonic and phasic motoneurons. Their findings identify differences in AZ organization, transcriptomic profiles, post-translational modifications, and Ca^{2+} dynamics that contribute to neuronal subtype synaptic diversity.

Highlights

Tonic and phasic motoneurons exhibit diversity in synaptic structure and output

Isoform-Patch-seq highlights differentially regulated molecular pathways

Genetic analyses identify regulators of Ca^{2+} buffering and AZ organization

Differential ubiquitination and sialylation regulate synaptic growth and structure

Jetti et al., 2023, Neuron , 1–16
November 15, 2023
https://doi.org/10.1016/j.neuron.2023.07.019

CellPress

Please cite this article in press as: Jetti et al., Molecular logic of synaptic diversity between *rosophila* tonic and phasic motoneurons, Neuron 2023), https://doi.org/10.1016/j.neuron.2023.07.019

Neuron

CellPress

Article

Molecular logic of synaptic diversity between *Drosophila* tonic and phasic motoneurons

Suresh K. Jetti,[1,*] Andrés B. Crane,[1] Yulia Akbergenova,[1] Nicole A. Aponte-Santiago,[1] Karen L. Cunningham,[1] Charles A. Whittaker,[2] and J. Troy Littleton[1,3,*]

[1]The Picower Institute for Learning and Memory, Department of Biology and Department of Brain and Cognitive Sciences, Massachusetts Institute of Technology, Cambridge, MA 02139, USA

[2]Koch Institute for Integrative Cancer Research, Massachusetts Institute of Technology, Cambridge, MA 02139, USA

[3]Lead contact

*Correspondence: sureshj@mit.edu (S.K.J.), troy@mit.edu (J.T.L.)

https://doi.org/10.1016/j.neuron.2023.07.019

SUMMARY

Although neuronal subtypes display unique synaptic organization and function, the underlying transcriptional differences that establish these features are poorly understood. To identify molecular pathways that contribute to synaptic diversity, single-neuron Patch-seq RNA profiling was performed on *Drosophila* tonic and phasic glutamatergic motoneurons. Tonic motoneurons form weaker facilitating synapses onto single muscles, while phasic motoneurons form stronger depressing synapses onto multiple muscles. Super-resolution microscopy and *in vivo* imaging demonstrated that synaptic active zones in phasic motoneurons are more compact and display enhanced Ca^{2+} influx compared with their tonic counterparts. Genetic analysis identified unique synaptic properties that mapped onto gene expression differences for several cellular pathways, including distinct signaling ligands, post-translational modifications, and intracellular Ca^{2+} buffers. These findings provide insights into how unique transcriptomes drive functional and morphological differences between neuronal subtypes.

INTRODUCTION

Although pathways driving neuronal development and function are well characterized, how diversity in neuronal subtypes across the brain is established and maintained is poorly understood. With the advent of single-cell transcriptomics, mRNA expression profiles that contribute to neuronal morphology, connectivity, and function are being identified.[1–4] One feature of diversity is the unique synaptic properties observed across neuronal classes. Synapses represent fundamental building blocks of information processing, exhibiting distinct synaptic vesicle (SV) release probability (P_r), response kinetics, and short-term plasticity.[5,6] Notable examples of synaptic diversity include *Caenorhabditis elegans* (*C. elegans*) AWC and ASH olfactory neurons,[7] invertebrate tonic and phasic motoneurons (MNs),[8] zebrafish ON and OFF bipolar cells,[9] and mammalian hippocampal, cerebellar, and auditory neurons.[5,10,11] Functional heterogeneity in synaptic transmission contributes to temporal coding, processing of multisensory information, and circuit computations.[12,13] Despite these roles, the differentially expressed genes (DEGs) that collectively specify differences in synaptic structure and output are largely unknown.

Neurons displaying tonic or phasic synaptic output are conserved from invertebrates to mammals and often co-innervate postsynaptic targets.[7,14,15] Tonic and phasic synapses increase the robustness of information processing by acting as high- and low-pass filters, respectively.[13,16] *Drosophila* larvae contain MNs with tonic or phasic output that co-innervate muscles and form glutamatergic neuromuscular junctions (NMJs).[8,14] Tonic MNs have bigger "type Ib" boutons and typically innervate single muscles to act as primary drivers of contraction.[17–19] Phasic MNs form smaller "type Is" boutons that innervate and coordinate contraction of muscle subgroups. Phasic MN active zones (AZs) display higher P_r and show synaptic depression during stimulation.[18,20–23] In contrast, tonic MNs have weaker synaptic output and undergo facilitation. Tonic and phasic MNs also show differences in morphology, inputs, membrane excitability, and synaptic plasticity.[24–27] The molecular logic that governs these differences is largely unknown, providing a system to characterize DEGs that establish and maintain these distinct properties.

In this study we combined single-neuron Patch-seq RNA profiling with quantal imaging, stimulated emission depletion (STED) nanoscopy, transmission electron microscopy (TEM), optogenetics, electrophysiology, and genetic manipulations to identify and dissect molecular components contributing to the structural and functional diversity of *Drosophila* tonic and phasic MNs. RNA sequencing (RNA-seq) identified distinct transcriptional profiles for each MN subtype, while genetic analyses indicate multiple DEGs contribute to functional and morphological differences in AZ organization, P_r, and Ca^{2+} buffering.

Please cite this article in press as: Jetti et al., Molecular logic of synaptic diversity between *rosophila* tonic and phasic motoneurons, Neuron 2023), https://doi.org/10.1016/j.neuron.2023.07.019

RESULTS

Tonic and phasic MNs exhibit diversity in morphology and synaptic properties

The *Drosophila* larval motor system contains glutamatergic (tonic type Ib and phasic type Is) and neuromodulatory (type II and III) MNs that control locomotion. In each abdominal hemisegment, 30 Ib MNs individually innervate the 30 body wall muscles, while two Is MNs innervate the dorsal or ventral muscles. Ib and Is MNs display differences in excitability, morphology, and synaptic strength.[14] We quantified their structural and functional synaptic properties as a foundation for characterizing DEGs that regulate these features. We focused on MN1-Ib (anterior corner cell [aCC]) that innervates muscle 1 and MNISN-Is (RP2, hereafter referred to as Is) that innervates dorsal muscles 1, 2, 3, 4, 9, 10, 11, 19, and 20 (Figure 1A), as available Gal4 drivers for these neurons facilitate cell-type-specific manipulations (Figure S1A).[20,28] MN1-Ib innervating muscle 1 and MN4-Ib innervating muscle 4 have similar properties, and comparisons of MN4-Ib with Is were performed in some experiments as segregation of their synaptic arbors facilitated imaging studies.

To quantify MN1-Ib and Is terminal morphology, synaptic NMJ area and AZ number were assayed at third-instar NMJs (Figures S1B–S1E). MN1-Ib had bigger boutons and a 4.4-fold larger NMJ field with 3.8-fold more AZs compared with Is at muscle 1 ($p < 0.0001$). However, when all postsynaptic muscles innervated by the dorsal Is were included, the total synaptic area of Is was 4.6-fold larger with 4.2-fold more AZs ($p < 0.0001$). To examine dendritic inputs, the electron microscopy (EM) connectome of abdominal segment one in the first-instar larval ventral nerve cord (VNC) was analyzed.[24,29,30] The dendrites of MN1-Ib bifurcate into ipsilateral and contralateral branches and contain 201 input synapses from 31 upstream neurons, while the Is dendritic arbor is confined to the ipsilateral side of the VNC with 137 input synapses from 21 neurons at this developmental stage (Figure 1B). MN1-Ib and Is receive inputs from both shared and distinct pre-motor and interneuron pools that drive their sequential recruitment during locomotion.[29,31,32] In summary, MN1-Ib has 75% fewer output synapses and 50% more input synapses than the dorsal Is, indicating that the transcriptomes of each MN subtype must support distinct synaptic development and maintenance requirements.

To assay presynaptic output, UAS-Channelrhodopsin-2 was expressed with MN1-Ib- or Is-specific Gal4 drivers and wide-field optogenetic NMJ stimulation was performed. Optically evoked excitatory junction potentials (EJPs) at muscle 1 were 54% larger following Is stimulation compared with Ib ($p < 0.01$, Figures 1C and 1D), consistent with prior studies.[21] Quantal imaging was performed using myristoylated-GCaMP7s to examine synaptic output at individual AZs. Expression of this genetically encoded Ca^{2+} indicator allowed detection of single SV fusion events at defined AZs.[33] Similar to recent studies,[18,34] Is AZs showed a 1.6-fold higher P_r than Ib AZs ($p < 0.0001$, Figures 1E–1G). Is MNs also had a smaller population of functionally silent AZs (Is, 5.6%; Ib, 17.1%, $p < 0.001$) and a higher P_r ceiling for the strongest release sites ($p < 0.02$, Figure 1H). To assay presynaptic Ca^{2+} influx at Ib and Is AZs, MNs were stimulated at 5 Hz in transgenic larvae expressing GCaMP7s fused to the N terminus of the AZ protein Bruchpilot (Brp), which resides near presynaptic voltage-gated Ca^{2+} channels (VGCCs) encoded by *Cacophony* (Cac).[35] Is AZs displayed 46% more presynaptic Ca^{2+} influx than Ib ($p < 0.0001$, Figures 1I and 1J). To determine whether elevated Ca^{2+} influx was secondary to more Ca^{2+} channels, quantification of CRISPR-tagged Cac-GFP AZ abundance was performed. A 13% reduction in Cac channels was observed at Is AZs ($p < 0.0001$, Figure 1K), indicating that Is AZs display greater Ca^{2+} influx and higher P_r despite having fewer Cac channels.

The nanoscopic organization of Ib and Is AZs are distinct

Drosophila AZs include a mushroom-shaped structure composed of Brp and other scaffolding proteins that appear as an electron-dense T-bar in TEM and a ring-like donut after STED imaging of Brp.[36] To assay structural differences between Is and Ib AZs, Brp immunostaining and STED were performed. Unlike the larger Brp rings observed in Ib, Is AZs displayed a triangular appearance (Figure 2A) with a reduced circularity index (CI) ($p < 0.0001$, Figure 2B) and a 37% smaller area ($p < 0.0001$, Figure 2C). To examine Ca^{2+} channel distribution, dual-color STED imaging was performed for Brp and GFP-tagged endogenous Cac.[37] Cac channel distribution was not significantly different (Figures 2D and 2E), and an increased Brp area correlated with a larger Cac area for both Ib and Is AZs (Figure 2F).

Given that Brp helps recruit SVs to AZs,[38] the distinct Brp AZ architecture might alter the number or distribution of SVs at release sites. To quantify SV distribution and AZ ultrastructure, TEM of third-instar larval Ib and Is synaptic boutons was performed (Figure 2G). Consistent with the smaller Brp area, T-bar length was 33% shorter at Is AZs ($p < 0.001$, Figure 2H). As previously described,[39] SVs in Is boutons were 30% larger than those at Ib synapses ($p < 0.0001$, Figure 2I). In spite of higher P_r, Is AZs contained fewer docked SVs within 40 nm of the electron-dense synaptic cleft ($p < 0.001$, Figure 2J) and less SVs clustered within 100–200 nm of the T-bar ($p < 0.0001$, Figure 2K). In addition, Ib MNs had a 2-fold increase in overall SV density within synaptic boutons ($p < 0.01$, Figure 2L), suggesting greater potential for sustained release to support their tonic output. If the distinct morphology of Ib and Is AZs contributes to P_r differences, the two MN subtypes might display differential sensitivity to Brp disruption. To test Brp-dependent SV release, P_r mapping was performed in brp^{69} null mutants at Ib and Is NMJs. Although evoked release was reduced at both terminals in brp^{69}, Is AZs were slightly more resistant and maintained higher P_r than Ib AZs ($p < 0.001$, Figures 2M and 2N). These data suggest that baseline P_r is Brp-dependent in both MN subtypes, with cell-type-specific P_r differences requiring factors in addition to Brp-mediated structural changes. Together, STED and TEM indicate that the nanoscale organization of the AZ cytomatrix and associated SV pools differs at Ib and Is AZs. Is AZs display higher P_r despite fewer docked SVs, suggesting that individual SV fusogenicity and greater Ca^{2+} influx contribute to enhanced release (Figure 2O).

Patch-seq RNA profiling identifies distinct transcriptional profiles for Ib and Is MNs

To examine pathways that establish these distinct synaptic properties, the transcriptomes of the two MN subtypes were

Please cite this article in press as: Jetti et al., Molecular logic of synaptic diversity between *rosophila* tonic and phasic motoneurons, Neuron 2023), https://doi.org/10.1016/j.neuron.2023.07.019

CellPress

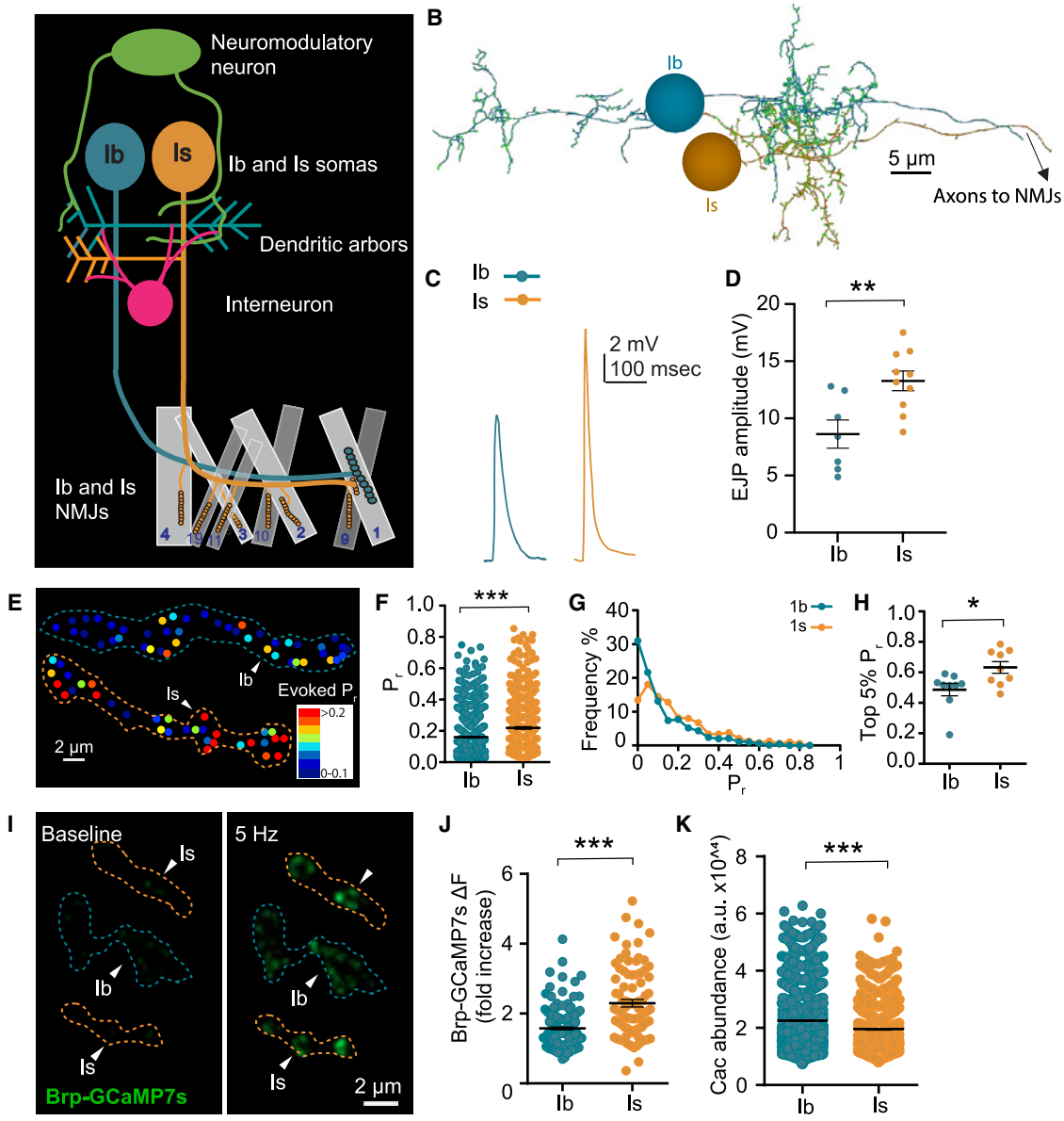

Figure 1. Synaptic differences in tonic Ib and phasic Is motoneurons

(A) Model of larval MN1-Ib and MNISN-Is. Somas are located in the VNC, with the Ib exclusively innervating muscle 1 while the Is innervates the dorsal muscle subgroup.

(B) EM reconstruction of MN1-Ib and MNISN-Is from first-instar abdominal segment A1. Synaptic inputs onto Ib and Is dendrites within the VNC are noted by green circles. Ib forms both ipsilateral and contralateral dendritic branches that cross the midline, while the Is dendritic arbor resides in the ipsilateral VNC.

(C) Representative EJP traces at third-instar muscle 1 evoked by optogenetic stimulation of MN1-Ib (R94G06-Gal4; UAS-ChR2^{T159C}) or Is (R27E09-Gal4; UAS-ChR2^{T159C}).

(D) Quantification of muscle 1 EJP amplitude for optical stimulation of Ib versus Is MNs (n = 7 larvae).

(E) Representative evoked AZ P_r heatmap at muscle 4 following quantal imaging of postsynaptic responses during 0.3 Hz stimulation.

(F) Quantification of P_r for Ib and Is AZs at muscle 4 NMJs from quantal imaging (Ib: 716 AZs from 9 NMJs, 4 larvae; Is: 476 AZs from 9 NMJs, 4 larvae).

(G) Histogram of single AZ P_r for Ib and Is NMJs at muscle 4.

(H) Quantification of average P_r for the strongest 5% of Ib or Is AZs at individual muscle 4 NMJs (n = 9 NMJs, 4 larvae).

(I) Representative images of resting (left) and 5-Hz-evoked (right) Ca^{2+} signals at Ib and Is NMJs at muscle 4 in larvae expressing Brp-GCaMP7s.

(J) Quantification of fold increase in Ca^{2+} levels during 5 Hz stimulation of Ib and Is NMJs at muscle 4 in larvae expressing Brp-GCaMP7s (Ib: n = 169 AZs from 7 NMJs, 3 larvae; Is: n = 87 AZs from 6 NMJs, 3 larvae).

(K) Quantification for Cac abundance (in a.u.) at Ib and Is AZs at muscle 4 (Ib: n = 1,600 AZs from 12 NMJs, 4 larvae; Is: n = 743 AZs from 12 NMJs, 4 larvae).

Data reports mean ± SEM. Student's t test, *p < 0.05, **p < 0.01, ***p < 0.001; ns, not significant.

Please cite this article in press as: Jetti et al., Molecular logic of synaptic diversity between *rosophila* tonic and phasic motoneurons, Neuron 2023), https://doi.org/10.1016/j.neuron.2023.07.019

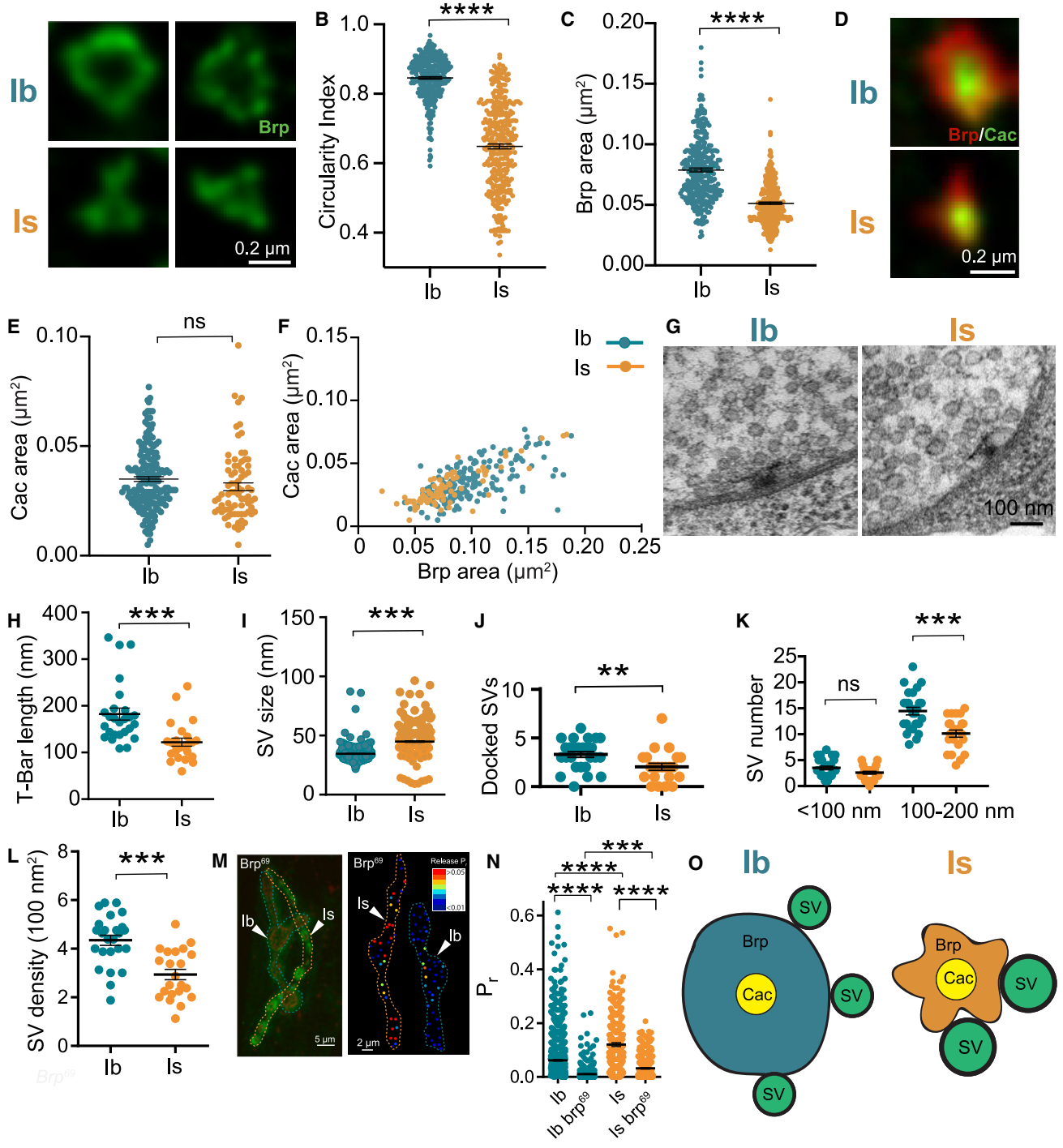

Figure 2. AZ nanoscopic diversity between Ib and Is AZs

(A) Representative STED images showing Ib (upper) and Is (lower) AZs immunolabeled with anti-Brp at muscle 4 NMJs in control w^{1118} third-instar larvae.

(B) Quantification of circularity index differences between Ib and Is AZs using STED at muscle 4 NMJs.

(C) Quantification of Brp area differences between Ib and Is AZs using STED at muscle 4 NMJs (n = 314 Ib AZs from 7 larvae and 345 Is AZs; 9 larvae for B and C).

(D) Representative STED images of endogenous CRISPR GFP-tagged Cac channels ($cac^{sfGFP\text{-}N}$) and Brp at Ib and Is AZs at muscle 4 NMJs.

(E) Quantification of Cac area at Ib and Is AZs using STED at muscle 4 NMJs.

(F) Quantification of Cac area vs. Brp area at Ib and Is AZs using STED at muscle 4 NMJs (n = 175 Ib AZs and 79 Is AZs from 4 larvae for E and F).

(G) Representative TEM images of Ib and Is T-bar organization in control third instars (w^{1118}).

(H) Quantification of T-bar length at Ib and Is AZs (Ib: n = 26 micrographs; Is: n = 24 micrographs).

(I) Quantification of SV diameter at Ib and Is synapses (Ib: n = 298 Ib SVs from 10 micrographs; Is: n = 338 Is SVs from 10 micrographs).

legend continued on next page)

Please cite this article in press as: Jetti et al., Molecular logic of synaptic diversity between *rosophila* tonic and phasic motoneurons, Neuron 2023), https://doi.org/10.1016/j.neuron.2023.07.019

compared. MN1-Ib and Is are among the first MNs born during embryogenesis and arise from distinct segmental neuroblast lineages. MN1-Ib, along with several interneurons and glia, derive from neuroblast NB1-1, while the Is and a few additional MNs and interneurons are descendants of neuroblast NB4-2. The initial transcriptional wave for synaptic genes occurs during embryogenesis from 12 to 24 h as the nervous system forms.[40] NMJ growth and AZ addition increase during the second- and third-instar stages,[33,41] and MNs continue to express genes required for maintaining their synaptic properties and populating new AZs.[42] Our synaptic studies were performed in third-instar larvae that are 5 days beyond embryogenesis, and we focused on characterizing Ib and Is transcriptomes during this developmental period.

Single-neuron Patch-seq RNA profiling was performed using a method modified from adult *Drosophila* neurons.[43] MN-Ib and -Is cells were labeled with GFP using specific Gal4 drivers to identify their cell bodies on the ventral surface of the third-instar VNC. RNA profiles for two postsynaptic partners, muscle 1 (innervated by MN1-Ib and Is) and muscle 4 (innervated by MN4-Ib and Is), were also determined. Cytosolic and nuclear content was extracted from individual cell bodies of 101 Is, 105 MN-Ib, and 35 muscles using whole-cell electrodes (Figure 3A). High-resolution paired-end deep single-cell RNA sequencing using Smart-seq 2 was then performed.[44] We termed this approach "Isoform-Patch-seq" as the method resulted in 4 million reads per cell and allowed identification of DEG profiles and splice isoform variants at single-cell resolution. Read counts for all genes and isoforms, along with a regularized logarithm transformation (rlog) in DeSeq2, is shown in Table S1.[45] Unsupervised hierarchical clustering and t-distributed stochastic neighbor embedding (tSNE) analyses indicated the transcriptomic profiles of MN-Ib, -Is, and muscles cluster into separate groups (Figure 3B). Comparison of the two MN populations identified 422 genes upregulated in Ib MNs and 402 genes upregulated in Is MNs, with an adjusted p value of < 0.05 (Figure 3C). A larger set of 5,000 DEGs were identified between MNs and muscles.

Isoform-Patch-seq identified 11 previously reported Ib and Is DEGs (*Proc*,[46] *hkb*,[47] *vGlut*,[48] *vvl*,[49] *DIP-* ,[50] *zfh1*,[51] *SiaT*,[52] *Toll-6*,[53] *pav*,[54] *pdm2*,[55] and *dpr4*[28]), in addition to many unknown DEGs. The 20 most statistically significant upregulated DEGs in Is MNs included those encoding the Ig domain containing axonal pathfinding proteins DIP-α and DIP-θ, the transcription factors (TFs) Huckebein (hkb) and Trachealess (trh), the Ca^{2+}-binding protein Calbindin 53E (Cbp53), the secreted glycoprotein Anachronism (ana) and serine protease Pegasus (CG17278), the synaptic cleft protein Hig, the intracellular transport protein p24-2, the actin-binding proteins Cib and Unc-115b, the microtubule-binding protein JPT1 (CG1943), the neuronal excitability regulator Julius Seizure (CG14509), the chaperone Hsp23, and the long non-coding RNA CR45924 (Figure 3D). Among the top 20 upregulated DEGs in Ib MNs were those encoding the cell-surface proteins Toll-6, Kek-3, Robo3, and Axotactin (axo); the signaling ligands Wnt4, Pyramus (fibroblast growth factor [FGF] ligand), and Eiger (tumor necrosis factor [TNF] ligand); the glutamate transporter Eaat1; the cyclin Cdk4; the dynein assembly factor Dnaaf3 (CG43737); the sialyltransferase ST6Gal (SiaT); the neuropeptide receptors AstC-R2 and Octβ3R; CNGL (cyclic nucleotide-gated ion channel-like); and the long non-coding RNA CR45139. CG3085 (encoding a tektin family cytoskeletal protein) and CG15537 (homologous to corticotropin-releasing hormone-binding protein) were Is-MN specific, while CG30457 (unknown function) and CG30098 (endopeptidase) were Ib-MN specific, showing binary ON/OFF expression between Is and Ib MNs. Isoform-Patch-seq also identified the major splice isoforms for every gene expressed in MNs, as well as splicing differences between MN1-Ib and Is (Table S2; Data S1). Although functional analysis of splicing differences will require further study, the glutamate receptor accessory protein Neto displayed differential isoform expression, with Neto-α being specifically upregulated in MN1-Ib. mRNAs encoding splice isoforms for two well-characterized AZ proteins, Brp^{short}/Brp^{long} and Unc13A/Unc13B, were not different between Ib and Is. Gene ontology (GO) analysis for all DEGs indicated synapse structure and function, along with proteasomal processing and developmental growth, were the most significant categories differentiating MN1-Ib and Is (Figure 3E).

To analyze protein expression for a subset of DEGs, immunofluorescence experiments were performed using GFP-protein-trap lines.[56] Prior studies found the Ig superfamily protein DIP-α labels Is MNs,[20,57] while the neurotrophin receptor Toll-6 marks 1b MNs.[53] Isoform-Patch-seq indicated enrichment of *DIP-* >63-fold in Is MNs and *Toll-6* 4-fold in Ib MNs. GFP trap lines confirmed cell-type-specific protein expression from these genes (Figures 3F and 3G). Trojan-Gal4 lines inserted within newly discovered DEGs also showed specific expression in Ib versus Is cells, as expected (Figures 3H, 3I, and S2). *Mayday* (CG31475, *myd*), encoding a Golgi-localized Ca^{2+}-binding protein,[58] was upregulated 6-fold in Is. A Mayday Trojan-Gal4 labeled both the dorsal and ventral Is MNs (Figure S2A). In contrast, *DIP-η* (>70-fold RNA enrichment in Is) was only expressed in the dorsal Is (Figures S2C and S2D), suggesting a role in synaptic targeting or maintenance for dorsal muscle NMJs. *Wnt4* (40-fold RNA increase in Ib) and *DIP-γ* (>3-fold RNA increase in Ib) were preferentially expressed in MN1-Ib and a few additional dorsal Ib MNs (Figures S2B, S2E, and

(J) Quantification of docked SVs at Ib and Is AZs (Ib: n = 26 micrographs; Is: n = 22 micrographs).
(K) Quantification of SV distribution around Ib and Is T-bars (Ib: n = 26 micrographs; Is: n = 22 micrographs).
(L) Quantification of SV density at Ib and Is boutons (Ib: n = 25 micrographs; Is: n = 22 micrographs).
(M) Representative image (left) and evoked P_r map (right) of quantal imaging with myristoylated-GCaMP7s at Ib and Is AZs in brp^{69} mutants at muscle 4 NMJs.
(N) Quantification for evoked P_r in control and brp^{69} mutants at muscle 4 NMJs (Con Ib: n = 1,047 AZs from 7 NMJs, 6 larvae; brp^{69} Ib: n = 502 AZs from 6 NMJs, 6 larvae; Con Is: n = 222 AZs from 6 NMJs, 6 larvae; brp^{69} Is: n = 301 AZs from 6 NMJs, 6 larvae). Data reports mean ± SEM. Student's t test, *p < 0.05, **p < 0.01, ***p < 0.001; ns, not significant.
(O) Model summarizing nanoscopic differences in Ib and Is AZ organization. Is AZs have bigger SVs, enhanced Ca^{2+} influx, and a smaller Brp cytomatrix compared with the larger Ib AZs. Data represents mean ± SEM. One-way ANOVA with Tukey correction was used to determine significance in (K) and (N). Student's t test was used for two bar graphs. *p < 0.05, **p < 0.01, ***p < 0.001, ****p < 0.0001; ns, not significant.

Please cite this article in press as: Jetti et al., Molecular logic of synaptic diversity between *rosophila* tonic and phasic motoneurons, Neuron 2023), https://doi.org/10.1016/j.neuron.2023.07.019

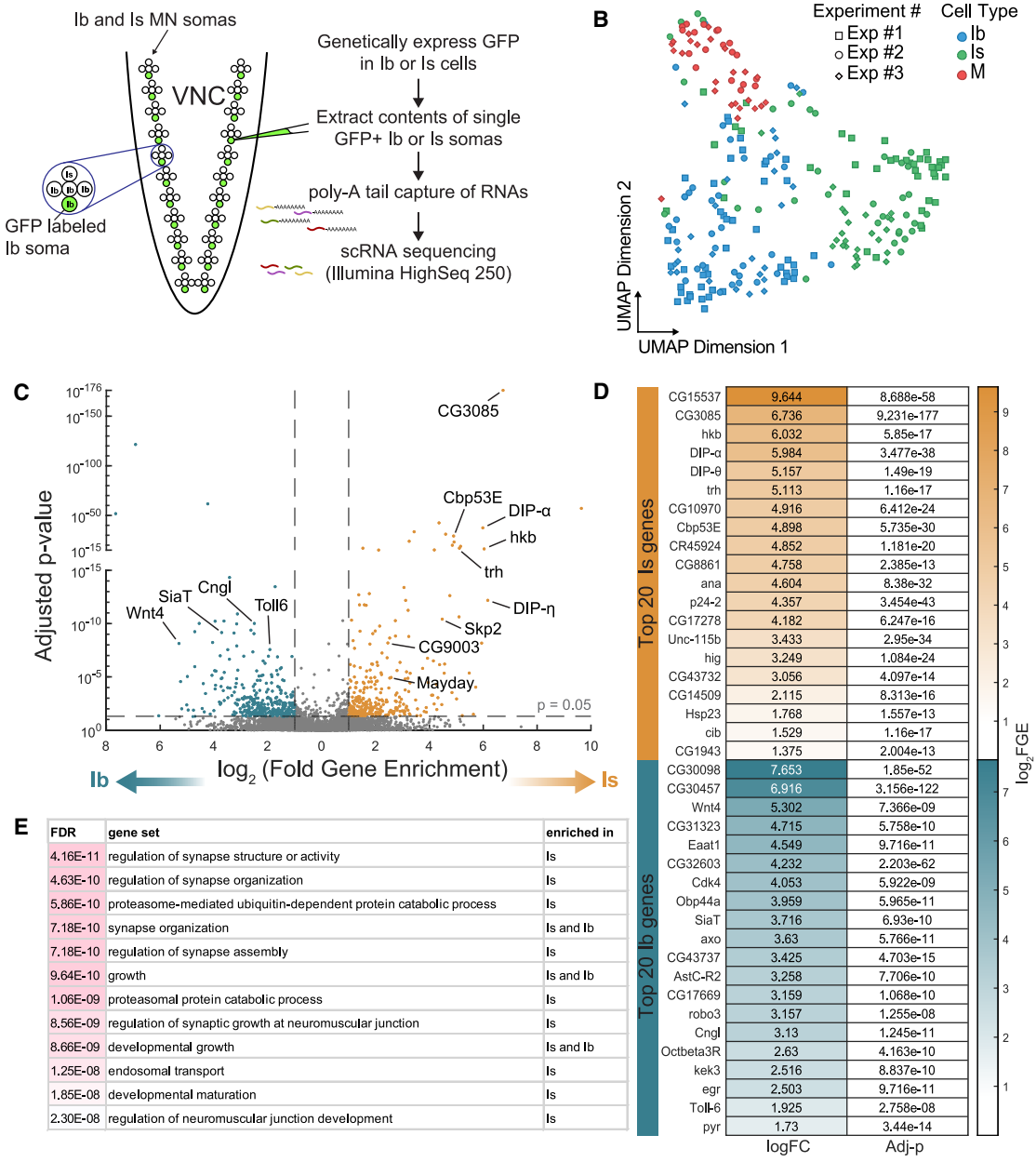

E

FDR	gene set	enriched in
4.16E-11	regulation of synapse structure or activity	Is
4.63E-10	regulation of synapse organization	Is
5.86E-10	proteasome-mediated ubiquitin-dependent protein catabolic process	Is
7.18E-10	synapse organization	Is and Ib
7.18E-10	regulation of synapse assembly	Is
9.64E-10	growth	Is and Ib
1.06E-09	proteasomal protein catabolic process	Is
8.56E-09	regulation of synaptic growth at neuromuscular junction	Is
8.66E-09	developmental growth	Is and Ib
1.25E-08	endosomal transport	Is
1.85E-08	developmental maturation	Is
2.30E-08	regulation of neuromuscular junction development	Is

Figure 3. Isoform-Patch-seq analysis of Ib and Is motoneurons

(A) Scheme for single MN Isoform-Patch-seq approach.

(B) Visualization of Ib and Is MNs compared with larval muscles 1 and 4 using t-distributed stochastic neighbor embedding (tSNE). Each dot represents a single MN or individual muscle coded in blue (Ib), green (Is), or red (muscle). Distinct experiments and sequencing runs are denoted by symbol shape (n = 101 Is MNs, 105 MN-Ibs, and 35 muscle samples).

legend continued on next page)

Please cite this article in press as: Jetti et al., Molecular logic of synaptic diversity between *rosophila* tonic and phasic motoneurons, Neuron 2023), https://doi.org/10.1016/j.neuron.2023.07.019

S2F). Together with confirmation of previously known DEGs, cell-type-specific labeling indicates that Isoform-Patch-seq differentiates Ib and Is transcriptomes. Although mRNA localization and translation rates influence protein production, and post-translational modifications (PTMs) regulate protein localization and turnover, these data provide a foundation for characterizing DEGs that contribute to distinct Is and Ib properties.

Analysis of Ib and Is MN transcriptomes

To further examine the transcriptional landscapes of Ib and Is, neuronal and synaptic gene classes[59] were assembled and analyzed (Table S3; Data S1). No differences were observed for genes encoding SV proteins and the fusion machinery. Although Is synapses contain larger SVs, endocytosis genes were similarly expressed, except for higher Epsin (Iqf) and Sorting Nexin 16 (Snx16) expression in Is. For genes encoding AZ proteins, RIM, RBP, and Teneurin-m (Ten-m) were upregulated in Is and previously shown to control AZ organization.[60–62] Multiple genes encoding synaptic cleft proteins were differentially expressed, including laminins and several secreted glycoproteins. mRNA for the acetylcholine receptor clustering protein Hig was enriched 10-fold in Is, suggesting unique postsynaptic organization. Among ionotropic neurotransmitter receptors, only the *nACHβ2* receptor gene was increased in MN1-Ib. No changes in voltage-gated Ca^{2+} or Na^{+} channel genes or their associated subunits were observed. Several K^{+} channel genes were upregulated in MN1-Ib, including *Shaw*, *Shab*, *SK*, *Ih*, and *CNGL*, while *KCNQ* was increased in Is. Multiple genes involved in ion balance and excitability were upregulated in Ib neurons (*Na^{+} pump β-subunit*, *Nhe2*, *Ncc69*, *Nckx30C*, *Kcc*, *vGlut*, *Eaat1*). More than 20 DEGs encoded G-protein and neuropeptide receptors, indicating MN1-Ib and Is are subject to distinct neuromodulation. 35 DEGs encoded proteins implicated in axonal pathfinding and synaptic targeting. Highly enriched pathfinding genes in Is included *DIP-η*, *DIP-θ*, *DIP- *, *Dpr2*, *Derailed* (*drl*), and *Fas2*, while MN1-Ib showed enrichment for *DIP-γ*, *Dpr4*, *Dpr10*, *Dpr18*, *Beat-IIb*, *Beat-IIIb*, and *Kek3*. Components regulating axonal transport (*Arl8*, *Unc-119*, and the kinesins *Unc-104* and *Pav*) and cytoskeletal organization (*Unc-115b*, *Cdc42*, *Cib*, *Mical*, *Jupiter*, *Rap1*, *Shot*, *-Tubulin84B*, *β-Tubulin56D*) were elevated in Is. Given that overexpression of Arl8 and Unc-104 increases synaptic cargo delivery in MNs,[63–65] alterations in rate-limiting transport machinery may enhance cargo delivery across the larger Is axonal arbors.

Although TFs driving early neuronal differentiation are unlikely to be present at the third-instar stage, MN1-Ib and Is continued to expressed unique TFs, including *Chinmo*, *Runt*, *Spalt major*, *Luna*, *Hormone-receptor-like 38*, and *Pangolin* in Ib, and *Trachealess*, *Huckebein*, *Zn finger homeodomain 1*, *Ventral veins lacking*, *Mamo*, *Sox14*, *Cap-n-collar*, and *Chip* in Is. Several DEGs encoded signaling proteins in MN1-Ib, including the bone morphogenetic protein (BMP) ligand *Mav*, the wingless ligand *Wnt4*, the FGF ligands *Branchless*, *Pyramus*, and *Thisbe*, the EGF superfamily ligands *Vein* and *Pvf2*, the Notch ligand *Weary*, and the TNF ligand *Eiger*. Downstream components of these signaling pathways were also differentially expressed, with *Toll-6*, the BMP-ligand-binding protein *Crimpy*, and the RhoGEF *Still life* (*sif*) upregulated in Ib, and *Dishevelled*, *Myopic*, *Trio*, *RohGEF2*, and *Spartin* upregulated in Is. Several mRNAs encoding kinome and phosphatome members were differentially expressed, including *CAMKII*, *PKA-R1*, *Pkn*, and *Cdi* upregulation in Is and enhanced *Pdk1*, *Lk6*, *p38a*, *Cdk4*, and *Eip63E* in Ib. These differences indicate that Ib and Is engage unique intracellular signaling pathways beyond their distinct synaptic output.

Genes encoding the core transcriptional and translational machinery were similarly expressed. No evidence for distinct energy requirements was identified at the transcriptional level, as mRNAs involved in mitochondrial function and metabolism were similar. Membrane trafficking components were mostly excluded from the DEGs, including SNAREs, Rabs, COPs, TRAPPs, CATCHRs, HOPS, Golgins, ESCRT, and Exocyst genes. The Retromer components *Snx3* and *Snx6* were upregulated in Is, along with the endoplasmic reticulum (ER)-Golgi transport regulator *p24-2*, whose mRNA was enriched 20-fold. Several autophagy genes were also increased in Is, including *Atg1* and *Atg4a*. Multiple mRNAs encoding proteins involved in PTMs were differentially expressed, with the *SiaT* sialytransferase that adds sialic acid to glycoproteins enriched 13-fold in Ib. In contrast, several genes encoding proteins implicated in ubiquitination and degradation were upregulated in Is. A matrix of mRNA expression levels for the 190 most robust DEGs in Ib and Is neurons is provided (Data S1).

Functional analysis of DEGs in Ib and Is MNs

To begin characterizing the functional relevance of Is and Ib DEGs, synaptic structure was assayed using available mutants and RNAi knockdown with the OK6 pan-MN Gal4 driver. Disruption of multiple DEGs resulted in Ib or Is synaptic growth defects at muscles 1 and/or 4 (Figure 4). Is bouton overgrowth was observed in RNAi knockdowns and mutants of several ubiquitin E3 ligases enriched in Is MNs (Figures 4A–4E and 4I), including the F-box proteins CG9003 ($p < 0.0001$) and Skp2 ($p < 0.01$), Ube4B ($p < 0.01$), and the E2 conjugating enzyme Ben ($p < 0.0001$). Although these genes are upregulated in Is, they are also expressed in Ib MNs, and

(C) Volcano plot of gene expression differences between MN1-Ib and Is, with each dot representing a single gene. Log_2 change (FC) and adjusted p values were plotted on the x and y axes, respectively. Genes upregulated in Ib and Is are color-coded in turquoise and orange.
(D) Heatmap of the top 20 DEGs in MN1-Ib and Is.
(E) Top gene ontology (GO) categories for DEGs enriched in Is or Ib MNs.
(F and G) Representative images of anti-GFP staining of larval VNCs in protein-trap lines for Is-enriched DIP-α (Mi{MIC}DIP-$\alpha^{MI02031}$) and Ib-enriched Toll-6 (Mi{MIC}Toll-$6^{MI02127}$). Elav immunostaining to label all neurons is shown in magenta.
(H and I) Representative images of anti-GFP staining of larval VNCs in Trojan-Gal4 lines for Is-enriched Mayday (Mi{Trojan-GAL4.2}myd$^{MI08258\text{-}TG4.2}$>10XUAS-IVS-mCD8::GFP) and Ib-enriched Wnt4 (Mi{Trojan-GAL4.2}Wnt4$^{MI03717\text{-}TG4.2}$>10XUAS-IVS-mCD8::GFP). Elav immunostaining to label all neurons is shown in magenta.

Please cite this article in press as: Jetti et al., Molecular logic of synaptic diversity between *rosophila* tonic and phasic motoneurons, Neuron 2023), https://doi.org/10.1016/j.neuron.2023.07.019

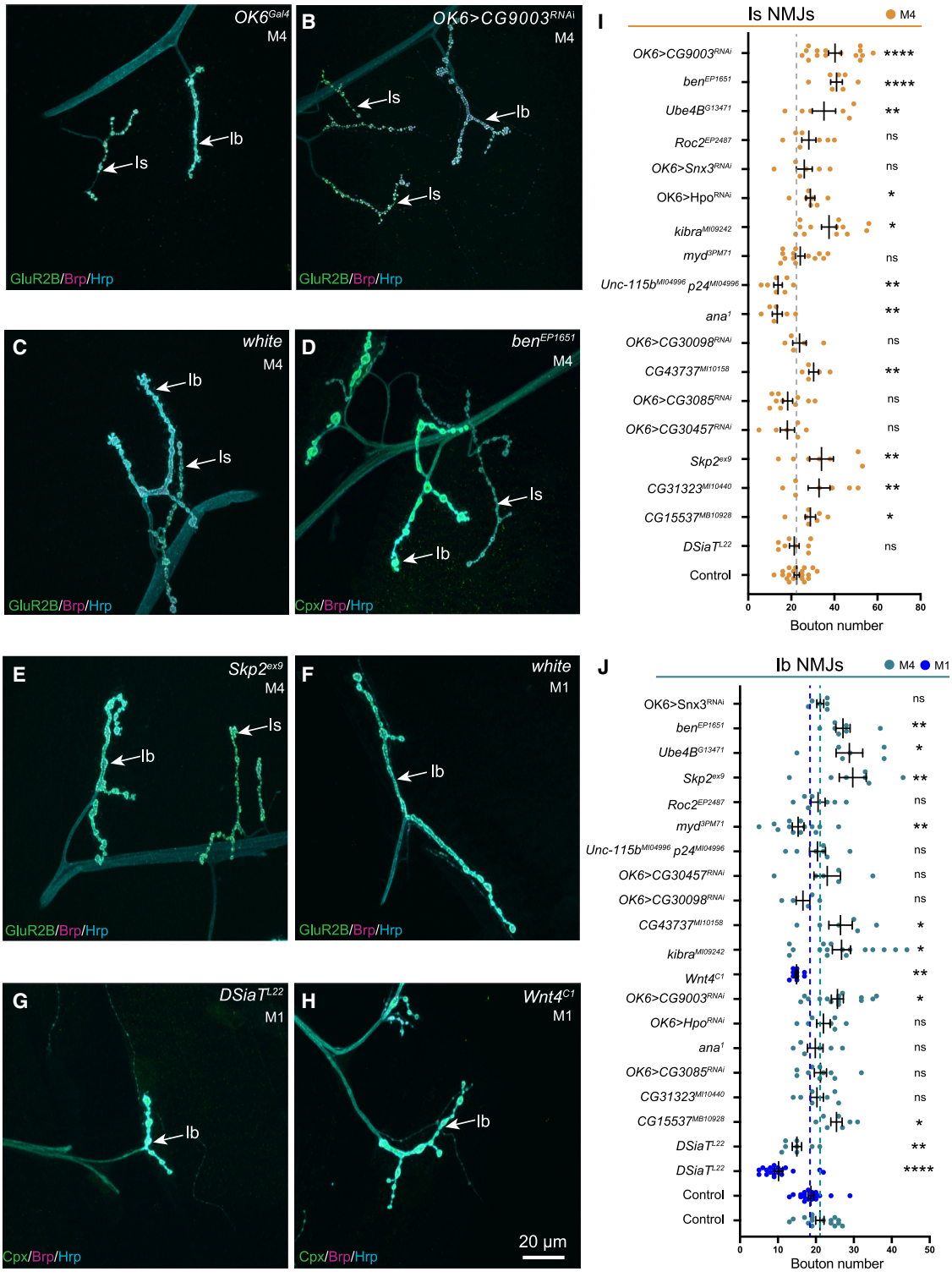

Figure 4. Morphological screen for synaptic growth defects following disruption of DEGs

(A–H) Representative confocal images of third-instar larval NMJs at muscle 1 (M1) or muscle 4 (M4) immunostained for GluR2B or complexin (green), Brp (magenta), and Hrp (cyan) for the indicated genotypes: (A) $OK6^{Gal4}$ control (M4), (B) $OK6^{Gal4}$>$CG9003^{RNAi}$ (M4), (C) w^{1118} control (M4), (D) ben^{EP1651} mutant (M4), (E) $Skp2^{exp}$ mutant (M4), (F) w^{1118} control (M1), (G) $DSiaT^{L22}$ mutant (M1), (H) $Wnt4^{C1}$ mutant (M1).

legend continued on next page)

Please cite this article in press as: Jetti et al., Molecular logic of synaptic diversity between *rosophila* tonic and phasic motoneurons, Neuron 2023), https://doi.org/10.1016/j.neuron.2023.07.019

disruptions of their function caused milder overgrowth at Ib NMJs (Figure 4J). Disruptions of the secreted glycoprotein Ana ($p < 0.01$, Figure 2I) and the transport regulator p24-2 ($p < 0.01$, Figure 2I) caused synaptic undergrowth at Is NMJs. Mutations in Kibra (a regulator of Hippo signaling) displayed overgrowth of both Is and Ib NMJs ($p < 0.05$, Figures 4I and 4J). Ib-specific synaptic undergrowth was observed in mutants disrupting *SiaT* ($p < 0.0001$, Figures 4G and 4J), the gene encoding the sole sialyltransferase that mediates sialylation of the cell surface and ECM proteome.[66] *Wnt4* mRNA was increased 40-fold in Ib MNs, with prior work suggesting a role in synapse specificity.[67] *Wnt4* mutants showed reduced synaptic growth at Ib terminals ($p < 0.01$, Figures 4H and 4J), indicating a role in Ib axonal arbor growth.

Given the role of the cytoskeleton in AZ organization,[68,69] STED was used to analyze the nanoscopic structure of Ib and Is AZs following disruption of several DEGs linked to cytoskeletal function. The Is-specific CG3085 protein encodes a *Drosophila* tektin. Tektins are enriched in neurons and regulate microtubule stability in other species.[70,71] CG3085 RNAi knockdown with OK6-Gal4 disrupted AZ structure in an Is-specific manner ($p < 0.0001$, Figures S3A and 3B). Although the donut-like organization of Ib AZs was unchanged, Is AZs were elongated, with reduced circularity. The Ib-enriched Toll-6 neurotrophin receptor controls microtubule dynamics at NMJs.[53,54] *Toll-6* null mutants reduced Ib AZ circularity ($p < 0.0001$, Figures S3C and S3D) without affecting Is AZs, suggesting cell-type-specific cytoskeletal regulation contributes to tonic and phasic MN development.

Distinct post-translational modifications regulate NMJ growth and AZ structure

Patch-seq suggested unique PTMs impact synaptic development in a cell-type-specific manner, while disruption of several of these DEGs altered synaptic growth (Figure 4). The Is-enriched F-box protein CG9003 is predicted to function in the Skp1-Cullin-F-box (SCF) E3 ligase complex by defining target specificity for ubiquitination, though its precise substrates are unknown.[72] CG9003 RNAi knockdown[73] and *SiaT* mutants[52] have reduced evoked responses at NMJs, indicating a functional role for ubiquitination and sialylation. *SiAT* mutants displayed reduced AZ number ($p < 0.0001$, Figure 5A) and synaptic area ($p < 0.0001$, Figure 5B) at Ib NMJs compared with controls or mutant Is NMJs (Figurse 5A–5C), indicating a preferential role for sialylation in arbor growth of tonic MNs. Beyond CG9003 and Skp2, multiple ubiquitin pathway components were upregulated in Is, including Roc2, Cul5, Posh, and the ubiquitin ligases Ube4B, CG2993, CG3014, and LUBEL (Figure S4), suggesting that phasic MNs employ a distinct ubiquitin code to regulate their synaptic properties. To explore this pathway, CG9003 was assayed in greater detail. Quantitative real-time PCR from adult heads demonstrated an 83% and 64% reduction in CG9003 mRNA levels in Tubulin-Gal4>UAS-CG9003 RNAi animals compared with Gal4 or RNAi controls. Pan-MN knockdown of CG9003 resulted in increased AZ number (OK6-Gal4 vs. OK6>CG9003^{RNAi}: $p < 0.01$; CG9003^{RNAi} vs. OK6>CG9003^{RNAi}: $p < 0.0001$, Figure 5D) and synaptic area (OK6-Gal4 vs. OK6>CG9003^{RNAi}: $p < 0.05$; CG9003^{RNAi} vs. OK6>CG9003^{RNAi}: $p < 0.0001$, Figure 5E) in Is MNs, with no effect at Ib NMJs (Figure 5D–5F). In mushroom body (MB) neurons, GC9003 functions with the supernumerary limbs (Slmb) F-box protein to regulate dendrite pruning.[72] Like CG9003, *Slmb* knockdown increased Is bouton and AZ number (Figures S5A–S5E), indicating that the two F-box proteins also regulate axonal growth (Figure 5G).

To determine whether differential PTMs contribute to Ib and Is AZ structure, STED was performed in *SiaT* mutants and CG9003 knockdowns. CG9003 knockdown disrupted the triangular organization of Is AZs, causing an increase in circularity ($p < 0.0001$, Figures 6A–6C) without affecting Ib AZs. In contrast, the donut-like organization of Ib AZs was disrupted in *SiaT* mutants with reductions in AZ area and circularity ($p < 0.0001$, Figures 6D–6F), indicating that sialylation regulates Ib AZ organization.

Cbp53E contributes to resting [Ca^2] differences and regulates paired-pulse facilitation

Cbp53E encodes a six EF-hand containing protein and is the homolog of vertebrate calbindin and calretinin proteins that act as Ca^{2+} buffers. Given that Cbp53E is enriched 30-fold in Is versus Ib MNs, differences in Cbp53E-mediated Ca^{2+} buffering might contribute to Is-specific Ca^{2+} regulation. To test this hypothesis, Ca^{2+}imaging was performed in control and *Cbp53E* mutants using AZ-targeted Brp-GCaMP7s (Figures 7A–7E). Brp-GCaMP7s fluorescence alone (Figure 7B) or normalized to AZ Brp levels (Figure 7C) were acquired. Resting Ca^{2+} levels were 27% higher at Ib AZs compared with Is in controls ($p < 0.0001$). The difference in resting [Ca^{2+}] was abolished in *Cbp53E* mutants, which showed no change in [Ca^{2+}] at Ib AZs and enhanced resting [Ca^{2+}] in Is (control Is vs. *Cbp53E* Is: $p < 0.001$; *Cbp53E* Ib vs. *Cbp53E* Is: $p = 0.94$, Figures 7B and 7C). *Cbp53E* mutants did not alter evoked Ca^{2+} influx at Is AZs (Figures 7D and 7E), indicating that other factors contribute to the enhanced Ca^{2+} influx at Is terminals. To determine whether Cbp53E-mediated Ca^{2+} buffering regulates presynaptic output, electrophysiology was performed at muscle 4 NMJs in *Cbp53E* mutants (Figures 7F–7H). Although initial evoked responses were not reduced, the response to a 2nd paired stimuli was enhanced across multiple time points (25, 50, and 75 ms). Given that Is terminals typically depress during paired-pulse stimulation, the enhanced facilitation in *Cbp53E* mutants indicates that Cbp53E-mediated Ca^{2+} buffering contributes to short-term plasticity, similar to the effects of Calbindin on facilitation at mammalian synapses.[74]

DISCUSSION

In this study, we describe the nanoscopic, transcriptomic, and post-translational signatures that contribute to distinct features

(I) Quantification of Is bouton growth for controls and the indicated mutants or RNAi knockdowns at larval muscle 4.
(J) Quantification for Ib bouton growth for controls and the indicated mutants or RNAi knockdowns at larval muscle 1 (M1) or 4 (M4).
Data represents mean ± SEM (n = 6–16 NMJs from 3 to 8 larvae for all genotypes in I and J). Student's t test, *$p < 0.05$, **$p < 0.01$, ***$p < 0.001$, ****$p < 0.0001$; ns, not significant.

Please cite this article in press as: Jetti et al., Molecular logic of synaptic diversity between *rosophila* tonic and phasic motoneurons, Neuron 2023), https://doi.org/10.1016/j.neuron.2023.07.019

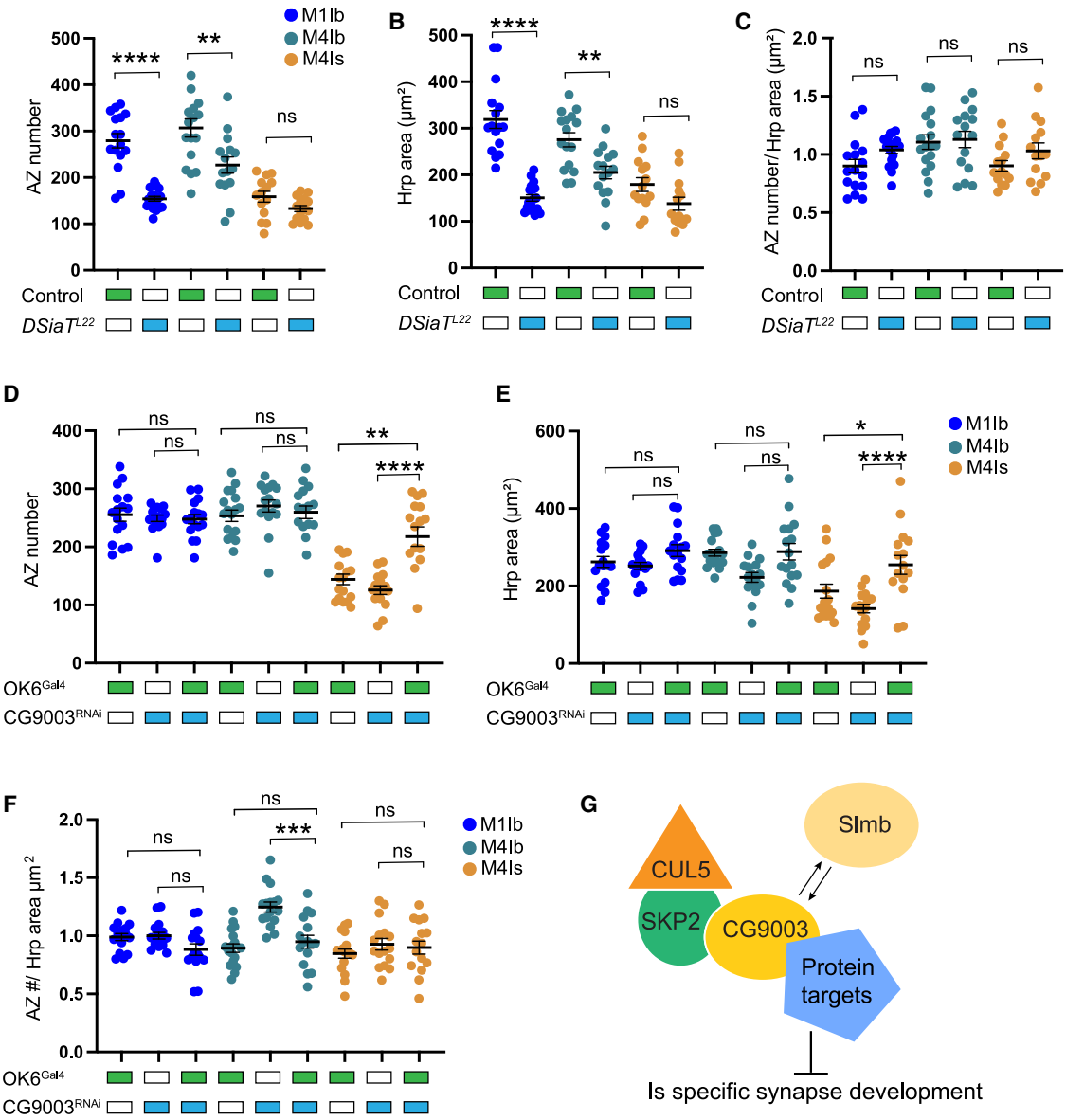

Figure 5. Differential PTMs regulate Ib and Is NMJ growth and AZ number

(A) Quantification of reduced Ib AZ number at muscle 1 and 4 NMJs in *DSiaT*^{L22} mutants compared with *w*^{1118} controls.
(B) Quantification of reduced Ib synapse area measured by HRP immunostaining in *DSiaT*^{L22} compared with *w*^{1118} control.
(C) Quantification of AZ number/area in *DSiaT*^{L22} mutants and *w*^{1118} controls.
(D) Quantification of enhanced Is AZ number in *OK6*^{Gal4}>CG9003^{RNAi} compared with controls of OK6^{Gal4} and UAS-CG9003^{RNAi} alone.
(E) Quantification of Is synapse area measured by HRP immunostaining in *OK6*^{Gal4}>*CG9003*^{RNAi} compared with controls of OK6^{Gal4} and UAS-CG9003^{RNAi} alone.
(F) Quantification of AZ number/area in *OK6*^{Gal4}>*CG9003*^{RNAi} compared with controls of OK6^{Gal4} and UAS-CG9003^{RNAi} alone.
(G) Model of the SKP2-CG9003-SCF ubiquitin ligase complex and its role in inhibiting Is synaptic growth.
Data represents mean ± SEM (n = 15 NMJs from 8 larvae for A–F in muscle 1 [M1] or muscle 4 [M4], as indicated). One-way ANOVA with Tukey correction was used to determine significance. *p < 0.05, **p < 0.01, ***p < 0.001, ****p < 0.0001; ns, not significant.

of tonic and phasic MN synaptic diversity. We identified a compact AZ structure and enhanced Ca^{2+} entry at phasic Is synapses. Our transcriptomic analysis revealed 800 DEGs that likely support differences in neuronal properties between the MN subtypes, including Cbp53E, which regulates resting [Ca^{2+}], the cytoskeletal regulators CG3085 and Toll-6, which contribute to AZ nanostructure, and the Wnt4 ligand, which participates in MN-specific synaptic growth programs. In addition, DEGs controlling sialylation and ubiquitination altered synaptic growth and AZ organization in a MN-specific manner. Genes

Please cite this article in press as: Jetti et al., Molecular logic of synaptic diversity between *rosophila* tonic and phasic motoneurons, Neuron 2023), https://doi.org/10.1016/j.neuron.2023.07.019

CellPress

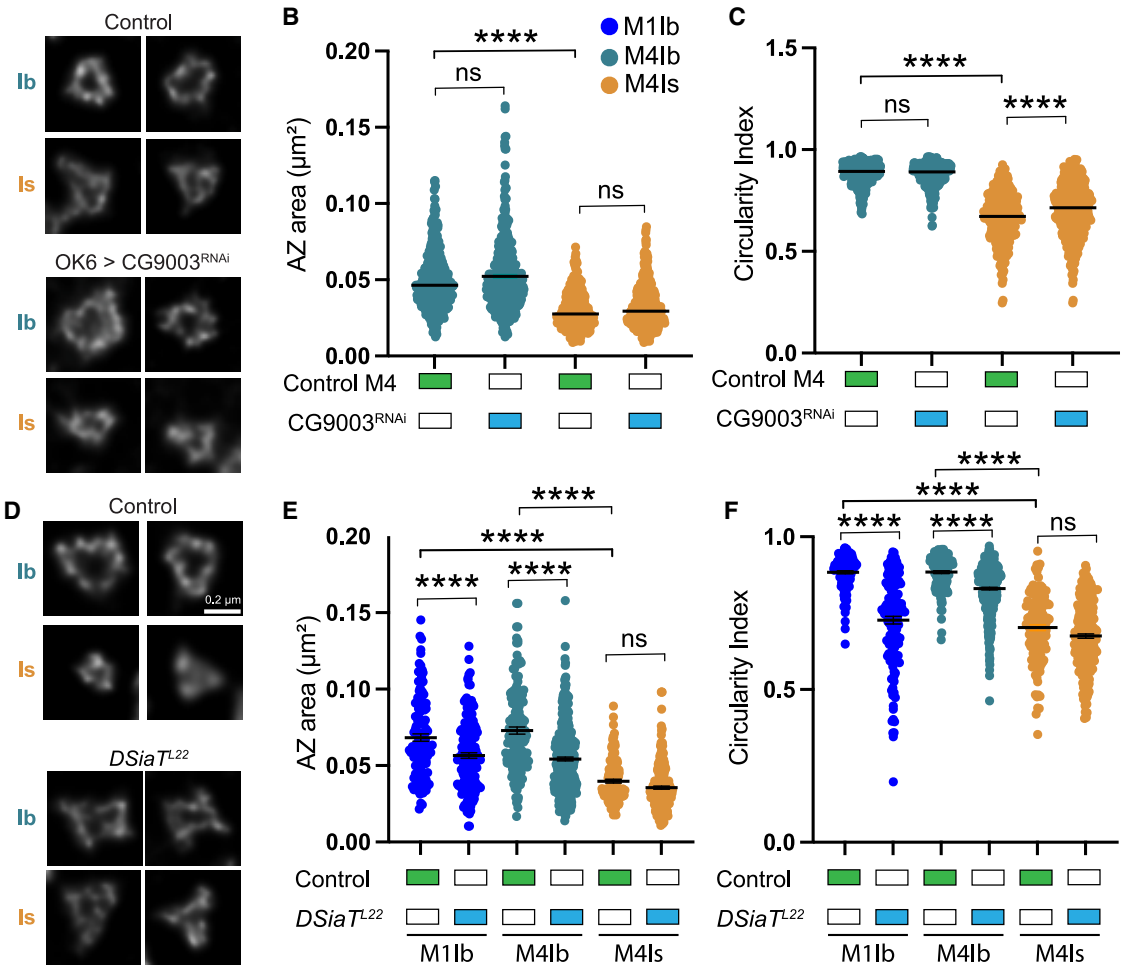

Figure 6. Differential PTMs regulate AZ nanoscopic structure

(A) Representative STED images of Ib and Is AZs at third-instar larval muscle 4 NMJs following anti-Brp immunolabeling in OK6^{Gal4} control (upper) and *OK6^{Gal4}*-Gal4>CG9003 RNAi (lower).

(B) Quantification of Brp area in OK6^{Gal4} control and *OK6^{Gal4}*>CG9003^{RNAi} at muscles 4 NMJs.

(C) Quantification of circularity index differences between control and OK6>CG9003^{RNAi} at muscle 4 NMJs

(B and C) OK6^{Gal4} controls: n = 363 Ib AZs and 269 Is AZs from 8 larvae: *OK6^{Gal4}*>CG9003^{RNAi}: 428 Ib AZs and 368 Is AZs from 8 larvae.

(D) Representative STED images of Ib and Is AZs following anti-Brp immunolabeling in control *w*^{1118} (upper) and *DsiaT^{L22}* mutants (lower) at muscle 4 NMJs.

(E) Quantification of Brp area differences between control *w*^{1118} and *DsiaT^{L22}* at muscle 1 or muscle 4 NMJs as indicated.

(F) Quantification of AZ circularity index differences between control *w*^{1118} and *DsiaT^{L22}* at muscle 1 or muscle 4 NMJs as indicated.

(E and F) Control MN1-Ib: n = 124 AZs from 5 larvae; *DsiaT^{L22}* MN1-Ib: 164 AZs from 5 larvae; control MN4-Ib: n = 150 AZs from 5 larvae; *DsiaT^{L22}* MN4-Ib: 340 AZs from 8 larvae; control Is at M4: n = 132 AZs from 5 larvae; *DsiaT^{L22}* Is at M4: 234 AZs from 8 larvae.

Data represents mean ± SEM. One-way ANOVA with Tukey correction was used to determine significance. *p < 0.05, **p < 0.01, ***p < 0.001, ****p < 0.0001; ns, not significant.

encoding neuropeptide receptors, synaptic cleft proteins, axonal pathfinding and cell adhesion molecules, membrane excitability and ionic balance regulators, and the Arl8 and Unc-104 axonal transport factors, were also differentially expressed. Together, these data provide a framework for characterizing molecular mechanisms contributing to unique features of tonic and phasic synaptic diversity (Figure 7I).

Our analysis is consistent with a model in which AZ structural differences and altered Ca^{2+} entry and buffering contribute to release differences between Ib and Is MNs. Given that phasic Is synapses have enhanced synaptic strength and higher P_r, their unique stellate AZ architecture and smaller cytomatrix, together with shorter T-bars and larger SVs, could contribute to distinct AZ Ca^{2+} dynamics and alterations in coupling Ca^{2+} influx to SV fusion. Previous studies demonstrated that changes in the coupling distance between SVs and Ca^{2+} channels can alter synaptic strength at a number of synapse types.[75,76] Increased expression of the Cbp53E Ca^{2+} buffer in Is MNs lowers resting [Ca^{2+}] and restricts facilitation, which, together with enhanced Ca^{2+} influx, provides a synergistic

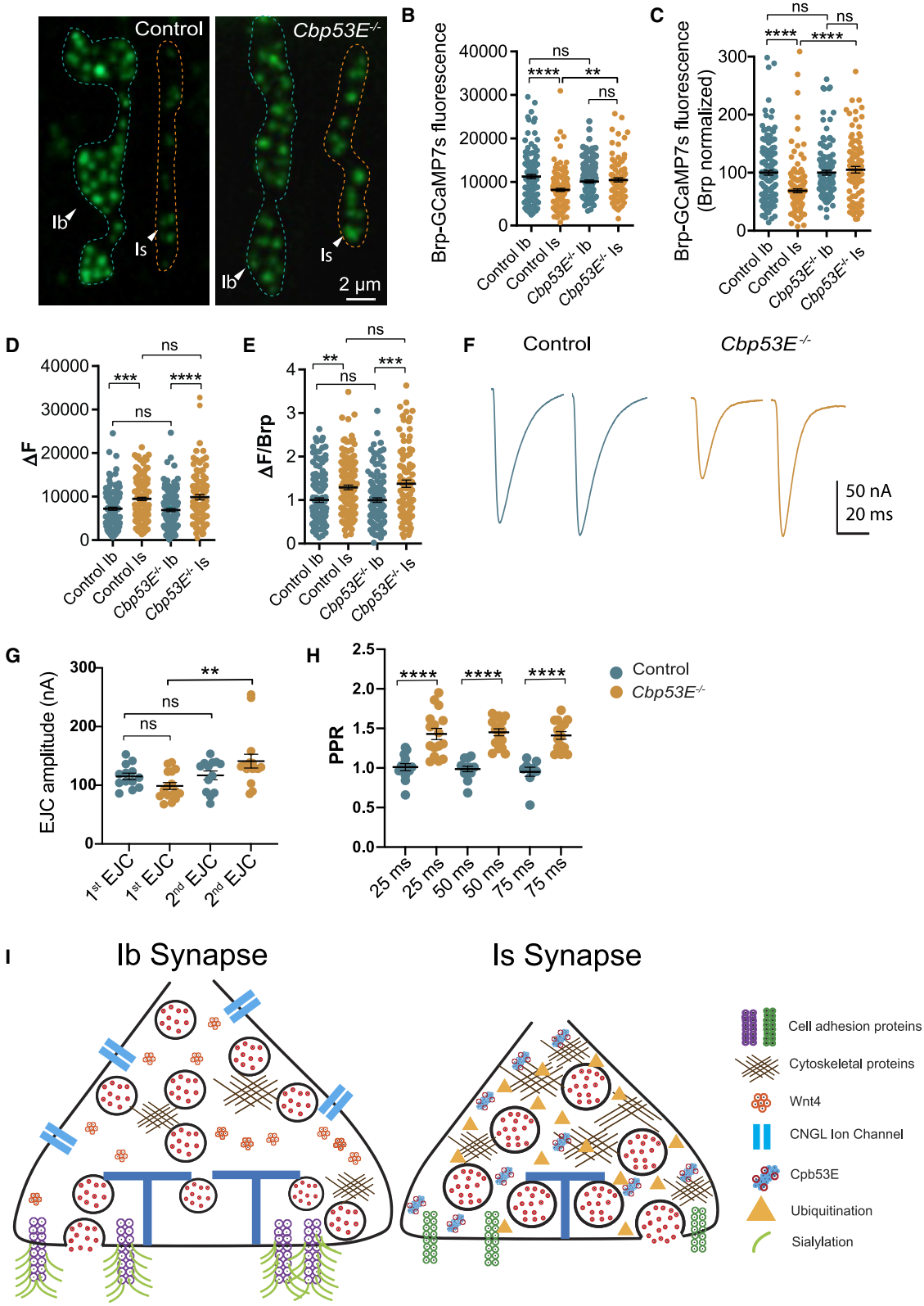

legend on next page)

Please cite this article in press as: Jetti et al., Molecular logic of synaptic diversity between *rosophila* tonic and phasic motoneurons, Neuron 2023), https://doi.org/10.1016/j.neuron.2023.07.019

mechanism with the more compact Is AZ nanostructure that could enhance release. Prior studies identified additional differences in SV availability and fusogenicity that also contribute to differences in Ib and Is release properties. Reduced expression of Brp, the decoy SNARE Tomosyn, and the fusion clamp Complexin at Is terminals alters the size of SV pools and their availability for fusion,[34,77–79] indicating that Ib synapses have fewer fusogenic SVs available to respond to Ca^{2+} entry, in part due to higher expression of these proteins. No changes in *Brp*, *Tomosyn*, or *Complexin* mRNA levels were detected in Isoform-Patch-seq, suggesting that post-translational degradation or altered trafficking underlies differences in their abundance at Is synapses.

Multiple studies indicate that PTMs, such as ubiquitylation, glycosylation, phosphorylation, acetylation, and sumoylation, impact synapse organization and function by modifying protein stability and localization.[80–83] Isoform-Patch-seq indicated that sialylation and ubiquitination are differentially regulated in Ib and Is MNs. Disruptions of other E3 ubiquitin ligases like Highwire alter synaptic growth at *Drosophila* NMJs, though they impact both Is and Ib terminals.[84] Identifying targets of the Skp2-CG9003 E3 ligase complex should clarify mechanisms by which cell-type-specific proteolysis contributes to synaptic morphology and function. Sialylation is critical for organization of the cell-surface proteome, regulation of cell adhesion, and control of neuronal excitability.[80,85] Lack of sialylation impairs surface expression of multiple ion channels and cell adhesion proteins, and further studies should identify the specific targets regulating Ib synaptic organization.

In summary, these data highlight multiple pathways that contribute to synaptic diversity between tonic and phasic MNs, while providing a resource to characterize additional DEGs that specify other structural and functional features of these neuronal subtypes. Neurons with tonic and phasic output represent an evolutionarily conserved design principle, and it will be interesting to determine whether similar DEGs are involved in other species. Recent RNA profiling indicates that *Drosophila* visual neurons differentially express sialyltransferases and proteolytic regulators,[86] while mammalian cortical GABAergic interneuron subtypes differentially express sialyltransferases that alter the cell-surface proteome.[87] As such, cell-type-specific PTMs may represent a widely used mechanism to generate neuronal diversity beyond their role in *Drosophila* tonic and phasic MNs.

STAR METHODS

Detailed methods are provided in the online version of this paper and include the following:

- KEY RESOURCES TABLE
- RESOURCE AVAILABILITY
  - Lead contact
  - Materials availability
  - Data and code availability
- EXPERIMENTAL MODEL AND STUDY PARTICIPANT DETAILS
  - *Drosophila* stocks
- METHOD DETAILS
  - Larval fillet preparation
  - Optogenetic stimulation
  - Sharp electrode current-clamp electrophysiology
  - Two-electrode voltage clamp electrophysiology
  - Isoform-Patch-seq protocol
  - Single-cell RNA library preparation and sequencing
  - Real-time PCR quantification of CG9003 RNAi knockdown
  - Synaptic GCaMP imaging
  - Immunohistochemistry of NMJ and CNS samples
  - Confocal imaging, image acquisition and processing
  - STED imaging
  - TEM sample preparation and imaging
  - Data exclusion criteria
  - Replication of results
- QUANTIFICATION AND STATISTICAL ANALYSIS
  - Electrophysiology data analysis
  - Synaptic GCaMP imaging data analysis
  - STED image analysis
  - Dataset Processing and Single-Sample Gene Set Enrichment Analysis
  - Differential gene expression analysis
  - Visualization and clustering of single-cell data
  - Gene ontology analysis

Figure 7. Increased resting [Ca^2] and enhanced paired-pulse facilitation in *Cbp5 E* mutants

(A) Representative images of resting Ca^{2+} fluorescence at Ib and Is NMJ AZs at muscle 4 in control w^{1118} and *Cbp53E* mutant larvae expressing Brp-GCaMP7s.

(B) Quantification of resting Ca^{2+} levels at Ib and Is AZs at muscle 4 in control w^{1118} and *Cbp53E* mutants expressing Brp-GCaMP7s.

(C) Quantification of resting Ca^{2+} levels normalized to AZ Brp abundance at Ib and Is AZs at muscle 4 in control w^{1118} and *Cbp53E* mutants expressing Brp-GCaMP7s.

(D) Quantification of fold increase in Ca^{2+} levels during 5 Hz stimulation of Ib and Is NMJs at muscle 4 in larvae expressing Brp-GCaMP7s in control w^{1118} and *Cbp53E* mutants.

(E) Quantification of fold increase in Ca^{2+} levels during 5 Hz stimulation of Ib and Is NMJs at muscle 4 normalized to AZ Brp abundance in control w^{1118} and *Cbp53E* mutants expressing Brp-GCaMP7s.

(B–E) Control: n = 135 Ib AZs and 139 Is AZs from 8 NMJs in 3 larvae; *Cbp53E*: n = 127 Ib AZs from 7 NMJs and 95 Is AZs from 6 NMJs in 3 larvae.

(F) Average paired-pulse excitatory junctional current (EJC) traces (50-ms inter-stimulus interval) at muscle 4 NMJs from control w^{1118} and *Cbp53E* mutants.

(G) Quantification of 1^{st} and 2^{nd} EJC amplitudes at muscle 4 NMJs in control w^{1118} (n = 13 NMJs, 9 larvae) and *Cbp53E* mutants (n = 16 NMJs, 9 larvae).

(H) Quantification of paired-pulse ratio (PPR) at muscle 4 NMJs at 25-, 50-, and 75-ms inter-stimulus intervals in control (w^{1118}, n = 13 NMJs, 9 larvae) and *Cbp53E* mutants (n = 16 NMJs, 9 larvae). One-way ANOVA with Tukey correction was used to determine significance. *p < 0.05, **p < 0.01, ***p < 0.001, ****p < 0.0001; ns, not significant.

(I) Model of Ib and Is synapses highlighting key differences identified in this study.

- RNAseq analysis, heatmaps, and violin plots
- Statistics and sample sizes

SUPPLEMENTAL INFORMATION

Supplemental information can be found online at https://doi.org/10.1016/j.neuron.2023.07.019.

ACKNOWLEDGMENTS

This work was supported by The JPB Foundation and NIH grants MH104536 and NS117588 to J.T.L. and F31NS118948 to A.B.C. K.L.C. and N.A.A.-S. were supported in part by NIH pre-doctoral training grant T32GM007287. We thank the Bloomington Drosophila Stock Center (NIH P40OD018537), the Developmental Studies Hybridoma Bank, the Vienna Drosophila Resource Center (Austria), Aaron DiAntonio (Washington University in St. Louis), Vladislav Panin (Texas A&M), Charles Tessier (Indiana School of Medicine), and Daniel Babcock (Lehigh University) for providing *Drosophila* strains and antibodies, Dina Volfson (MIT) for cloning assistance, Stuart Levine (MIT) for RNA-seq library and sequencing assistance, Mala Murthy and Amanda Crocker for technical advice on Patch-seq, Harvard Imaging Core for STED access, and members of the Littleton lab for helpful discussions on the manuscript.

AUTHOR CONTRIBUTIONS

Conceptualization, S.K.J. and J.T.L.; methodology, S.K.J., A.B.C., Y.A., N.A.A.-S., and C.A.W.; investigation, S.K.J., A.B.C., Y.A., and K.L.C.; funding acquisition, J.T.L.; supervision, J.T.L.; writing – original draft, S.K.J., A.B.C., and J.T.L.; writing – review & editing, S.K.J., A.B.C., Y.A., N.A.A.-S., K.L.C., and J.T.L.

DECLARATION OF INTERESTS

The authors declare no competing interests.

INCLUSION AND DIVERSITY

We support inclusive, diverse, and equitable conduct of research.

Received: January 17, 2023
Revised: May 22, 2023
Accepted: July 28, 2023
Published: August 22, 2023

REFERENCES

1. Belgard, T.G., Marques, A.C., Oliver, P.L., Abaan, H.O., Sirey, T.M., Hoerder-Suabedissen, A., García-Moreno, F., Molnár, Z., Margulies, E.H., and Ponting, C.P. (2011). A transcriptomic atlas of mouse neocortical layers. Neuron *71*, 605–616.
2. Darmanis, S., Sloan, S.A., Zhang, Y., Enge, M., Caneda, C., Shuer, L.M., Hayden Gephart, M.G., Barres, B.A., and Quake, S.R. (2015). A survey of human brain transcriptome diversity at the single cell level. Proc. Natl. Acad. Sci. USA *112*, 7285–7290.
3. Lake, B.B., Ai, R., Kaeser, G.E., Salathia, N.S., Yung, Y.C., Liu, R., Wildberg, A., Gao, D., Fung, H.L., Chen, S., et al. (2016). Neuronal subtypes and diversity revealed by single-nucleus RNA sequencing of the human brain. Science *352*, 1586–1590.
4. Corrales, M., Cocanougher, B.T., Kohn, A.B., Wittenbach, J.D., Long, X.S., Lemire, A., Cardona, A., Singer, R.H., Moroz, L.L., and Zlatic, M. (2022). A single-cell transcriptomic atlas of complete insect nervous systems across multiple life stages. Neural Dev. *17*, 8.
5. Dittman, J.S., Kreitzer, A.C., and Regehr, W.G. (2000). Interplay between facilitation, depression, and residual calcium at three presynaptic terminals. J. Neurosci. *20*, 1374–1385.
6. Millar, A.G., Bradacs, H., Charlton, M.P., and Atwood, H.L. (2002). Inverse relationship between release probability and readily releasable vesicles in depressing and facilitating synapses. J. Neurosci. *22*, 9661–9667.
7. Ventimiglia, D., and Bargmann, C.I. (2017). Diverse modes of synaptic signaling, regulation, and plasticity distinguish two classes of C. elegans glutamatergic neurons. eLife *6*, e31234.
8. Lnenicka, G.A., and Keshishian, H. (2000). Identified motor terminals in Drosophila larvae show distinct differences in morphology and physiology. J. Neurobiol. *43*, 186–197.
9. Odermatt, B., Nikolaev, A., and Lagnado, L. (2012). Encoding of luminance and contrast by linear and nonlinear synapses in the retina. Neuron *73*, 758–773.
10. Rollenhagen, A., and Lubke, J.H.R. (2006). The morphology of excitatory central synapses: from structure to function. Cell Tissue Res. *326*, 221–237.
11. Regehr, W.G. (2012). Short-term presynaptic plasticity. Cold Spring Harb. Perspect. Biol. *4*, a005702.
12. Chabrol, F.P., Arenz, A., Wiechert, M.T., Margrie, T.W., and DiGregorio, D.A. (2015). Synaptic diversity enables temporal coding of coincident multisensory inputs in single neurons. Nat. Neurosci. *18*, 718–727.
13. Abbott, L.F., and Regehr, W.G. (2004). Synaptic computation. Nature *431*, 796–803.
14. Aponte-Santiago, N.A., and Littleton, J.T. (2020). Synaptic properties and plasticity mechanisms of invertebrate tonic and phasic neurons. Front. Physiol. *11*, 611982.
15. Ellwood, I.T., Patel, T., Wadia, V., Lee, A.T., Liptak, A.T., Bender, K.J., and Sohal, V.S. (2017). Tonic or Phasic Stimulation of Dopaminergic Projections to Prefrontal Cortex Causes Mice to Maintain or Deviate from Previously Learned Behavioral Strategies. J. Neurosci. *37*, 8315–8329.
16. Jackman, S.L., and Regehr, W.G. (2017). The mechanisms and functions of synaptic facilitation. Neuron *94*, 447–464.
17. Johansen, J., Halpern, M.E., Johansen, K.M., and Keshishian, H. (1989). Stereotypic morphology of glutamatergic synapses on identified muscle cells of Drosophila larvae. J. Neurosci. *9*, 710–725.
18. Newman, Z.L., Hoagland, A., Aghi, K., Worden, K., Levy, S.L., Son, J.H., Lee, L.P., and Isacoff, E.Y. (2017). Input-Specific Plasticity and Homeostasis at the Drosophila Larval Neuromuscular Junction. Neuron *93*, 1388–1404.e10.
19. Hoang, B., and Chiba, A. (2001). Single-cell analysis of Drosophila larval neuromuscular synapses. Dev. Biol. *229*, 55–70.
20. Aponte-Santiago, N.A., Ormerod, K.G., Akbergenova, Y., and Littleton, J.T. (2020). Synaptic plasticity induced by differential manipulation of tonic and phasic motoneurons in Drosophila. J. Neurosci. *40*, 6270–6288.
21. Genç, Ö., and Davis, G.W. (2019). Target-wide Induction and Synapse Type-Specific Robustness of Presynaptic Homeostasis. Curr. Biol. *29*, 3863–3873.e2.
22. Karunanithi, S., Lin, Y.Q., Odierna, G.L., Menon, H., Gonzalez, J.M., Neely, G.G., Noakes, P.G., Lavidis, N.A., Moorhouse, A.J., and van Swinderen, B. (2020). Activity-Dependent Global Downscaling of Evoked Neurotransmitter Release across Glutamatergic Inputs in Drosophila. J. Neurosci. *40*, 8025–8041.
23. Lu, Z., Chouhan, A.K., Borycz, J.A., Lu, Z., Rossano, A.J., Brain, K.L., Zhou, Y., Meinertzhagen, I.A., and Macleod, G.T. (2016). High-Probability Neurotransmitter Release Sites Represent an Energy-Efficient Design. Curr. Biol. *26*, 2562–2571.
24. Zarin, A.A., Mark, B., Cardona, A., Litwin-Kumar, A., and Doe, C.Q. (2019). A multilayer circuit architecture for the generation of distinct locomotor behaviors in Drosophila. eLife *8*, e51781.
25. Lnenicka, G.A. (2020). Crayfish and drosophila nmjs. Neurosci. Lett. *732*, 135110.

26. Choi, J.C., Park, D., and Griffith, L.C. (2004). Electrophysiological and morphological characterization of identified motor neurons in the Drosophila third instar larva central nervous system. J. Neurophysiol. *91*, 2353–2365.
27. Couton, L., Mauss, A.S., Yunusov, T., Diegelmann, S., Evers, J.F., and Landgraf, M. (2015). Development of connectivity in a motoneuronal network in Drosophila larvae. Curr. Biol. *25*, 568–576.
28. Pérez-Moreno, J.J., and O'Kane, C.J. (2019). GAL4 drivers specific for type ib and type is motor neurons in drosophila. G3 (Bethesda) *9*, 453–462.
29. Schneider-Mizell, C.M., Gerhard, S., Longair, M., Kazimiers, T., Li, F., Zwart, M.F., Champion, A., Midgley, F.M., Fetter, R.D., Saalfeld, S., et al. (2016). Quantitative neuroanatomy for connectomics in Drosophila. eLife *5*, e12059.
30. Milyaev, N., Osumi-Sutherland, D., Reeve, S., Burton, N., Baldock, R.A., and Armstrong, J.D. (2012). The Virtual Fly Brain browser and query interface. Bioinformatics *28*, 411–415.
31. Zwart, M.F., Pulver, S.R., Truman, J.W., Fushiki, A., Fetter, R.D., Cardona, A., and Landgraf, M. (2016). Selective inhibition mediates the sequential recruitment of motor pools. Neuron *91*, 615–628.
32. Fushiki, A., Zwart, M.F., Kohsaka, H., Fetter, R.D., Cardona, A., and Nose, A. (2016). A circuit mechanism for the propagation of waves of muscle contraction in Drosophila. eLife *5*, e13253.
33. Akbergenova, Y., Cunningham, K.L., Zhang, Y.V., Weiss, S., and Littleton, J.T. (2018). Characterization of developmental and molecular factors underlying release heterogeneity at Drosophila synapses. eLife *7*, e38268.
34. Sauvola, C.W., Akbergenova, Y., Cunningham, K.L., Aponte-Santiago, N.A., and Littleton, J.T. (2021). The decoy SNARE Tomosyn sets tonic versus phasic release properties and is required for homeostatic synaptic plasticity. eLife *10*, e72841.
35. Kittel, R.J., Wichmann, C., Rasse, T.M., Fouquet, W., Schmidt, M., Schmid, A., Wagh, D.A., Pawlu, C., Kellner, R.R., Willig, K.I., et al. (2006). Bruchpilot promotes active zone assembly, Ca2+ channel clustering, and vesicle release. Science *312*, 1051–1054.
36. Fouquet, W., Owald, D., Wichmann, C., Mertel, S., Depner, H., Dyba, M., Hallermann, S., Kittel, R.J., Eimer, S., and Sigrist, S.J. (2009). Maturation of active zone assembly by Drosophila Bruchpilot. J. Cell Biol. *186*, 129–145.
37. Gratz, S.J., Goel, P., Bruckner, J.J., Hernandez, R.X., Khateeb, K., Macleod, G.T., Dickman, D., and O'Connor-Giles, K.M. (2019). Endogenous Tagging Reveals Differential Regulation of Ca^{2+} Channels at Single Active Zones during Presynaptic Homeostatic Potentiation and Depression. J. Neurosci. *39*, 2416–2429.
38. Matkovic, T., Siebert, M., Knoche, E., Depner, H., Mertel, S., Owald, D., Schmidt, M., Thomas, U., Sickmann, A., Kamin, D., et al. (2013). The Bruchpilot cytomatrix determines the size of the readily releasable pool of synaptic vesicles. J. Cell Biol. *202*, 667–683.
39. Karunanithi, S., Marin, L., Wong, K., and Atwood, H.L. (2002). Quantal size and variation determined by vesicle size in normal and mutant Drosophila glutamatergic synapses. J. Neurosci. *22*, 10267–10276.
40. Gerstein, M.B., Rozowsky, J., Yan, K.K., Wang, D., Cheng, C., Brown, J.B., Davis, C.A., Hillier, L., Sisu, C., Li, J.J., et al. (2014). Comparative analysis of the transcriptome across distant species. Nature *512*, 445–448.
41. Zito, K., Parnas, D., Fetter, R.D., Isacoff, E.Y., and Goodman, C.S. (1999). Watching a synapse grow: noninvasive confocal imaging of synaptic growth in Drosophila. Neuron *22*, 719–729.
42. Cunningham, K.L., Sauvola, C.W., Tavana, S., and Littleton, J.T. (2022). Regulation of presynaptic Ca2+ channel abundance at active zones through a balance of delivery and turnover. eLife *11*, e78648.
43. Crocker, A., Guan, X.J., Murphy, C.T., and Murthy, M. (2016). Cell-Type-Specific Transcriptome Analysis in the Drosophila Mushroom Body Reveals Memory-Related Changes in Gene Expression. Cell Rep. *15*, 1580–1596.
44. Trombetta, J.J., Gennert, D., Lu, D., Satija, R., Shalek, A.K., and Regev, A. (2014). Preparation of Single-Cell RNA-Seq Libraries for Next Generation Sequencing. Curr. Protoc. Mol. Biol. *107*, 4.22.1–4.22.17.
45. Love, M.I., Huber, W., and Anders, S. (2014). Moderated estimation of fold change and dispersion for RNA-seq data with DESeq2. Genome Biol. *15*, 550.
46. Nassel, D.R. (2018). Substrates for neuronal cotransmission with neuropeptides and small molecule neurotransmitters in *Drosophila*. Front. Cell. Neurosci. *12*, 83.
47. Chu-LaGraff, Q., Schmid, A., Leidel, J., Brönner, G., Jackle, H., and Doe, C.Q. (1995). *huckebein* specifies aspects of CNS precursor identity required for motoneuron axon pathfinding. Neuron *15*, 1041–1051.
48. Diao, F., Ironfield, H., Luan, H., Diao, F., Shropshire, W.C., Ewer, J., Marr, E., Potter, C.J., Landgraf, M., and White, B.H. (2015). Plug-and-play genetic access to *Drosophila* cell types using exchangeable exon cassettes. Cell Rep. *10*, 1410–1421.
49. Anderson, M.G., Perkins, G.L., Chittick, P., Shrigley, R.J., and Johnson, W.A. (1995). drifter, a *Drosophila* POU-domain transcription factor, is required for correct differentiation and migration of tracheal cells and midline glia. Genes Dev. *9*, 123–137.
50. Carrillo, R.A., Özkan, E., Menon, K.P., Nagarkar-Jaiswal, S., Lee, P.T., Jeon, M., Birnbaum, M.E., Bellen, H.J., Garcia, K.C., and Zinn, K. (2015). Control of synaptic connectivity by a network of *Drosophila* IgSF cell surface proteins. Cell *163*, 1770–1782.
51. Layden, M.J., Odden, J.P., Schmid, A., Garces, A., Thor, S., and Doe, C.Q. (2006). Zfh1, a somatic motor neuron transcription factor, regulates axon exit from the CNS. Dev. Biol. *291*, 253–263.
52. Repnikova, E., Koles, K., Nakamura, M., Pitts, J., Li, H., Ambavane, A., Zoran, M.J., and Panin, V.M. (2010). Sialyltransferase regulates nervous system function in Drosophila. J. Neurosci. *30*, 6466–6476.
53. McIlroy, G., Foldi, I., Aurikko, J., Wentzell, J.S., Lim, M.A., Fenton, J.C., Gay, N.J., and Hidalgo, A. (2013). Toll-6 and Toll-7 function as neurotrophin receptors in the Drosophila melanogaster CNS. Nat. Neurosci. *16*, 1248–1256.
54. McLaughlin, C.N., Nechipurenko, I.V., Liu, N., and Broihier, H.T. (2016). A Toll receptor-FoxO pathway represses Pavarotti/MKLP1 to promote microtubule dynamics in motoneurons. J. Cell Biol. *214*, 459–474.
55. McDonald, J.A., Fujioka, M., Odden, J.P., Jaynes, J.B., and Doe, C.Q. (2003). Specification of motoneuron fate in *Drosophila*: integration of positive and negative transcription factor inputs by a minimal eve enhancer. J. Neurobiol. *57*, 193–203.
56. Nagarkar-Jaiswal, S., DeLuca, S.Z., Lee, P.T., Lin, W.W., Pan, H., Zuo, Z., Lv, J., Spradling, A.C., and Bellen, H.J. (2015). A genetic toolkit for tagging intronic MiMIC containing genes. eLife *4*, e08469.
57. Ashley, J., Sorrentino, V., Lobb-Rabe, M., Nagarkar-Jaiswal, S., Tan, L., Xu, S., Xiao, Q., Zinn, K., and Carrillo, R.A. (2019). Transsynaptic interactions between IgSF proteins DIP-α and Dpr10 are required for motor neuron targeting specificity. eLife *8*, e42690.
58. Sidisky, J.M., Weaver, D., Hussain, S., Okumus, M., Caratenuto, R., and Babcock, D. (2021). Mayday sustains trans-synaptic BMP signaling required for synaptic maintenance with age. eLife *10*, e54932.
59. Littleton, J.T., and Ganetzky, B. (2000). Ion channels and synaptic organization: analysis of the Drosophila genome. Neuron *26*, 35–43.
60. Graf, E.R., Valakh, V., Wright, C.M., Wu, C., Liu, Z., Zhang, Y.Q., and DiAntonio, A. (2012). RIM promotes calcium channel accumulation at active zones of the Drosophila neuromuscular junction. J. Neurosci. *32*, 16586–16596.
61. Liu, K.S.Y., Siebert, M., Mertel, S., Knoche, E., Wegener, S., Wichmann, C., Matkovic, T., Muhammad, K., Depner, H., Mettke, C., et al. (2011). RIM-binding protein, a central part of the active zone, is essential for neurotransmitter release. Science *334*, 1565–1569.

62. Mosca, T.J., Hong, W., Dani, V.S., Favaloro, V., and Luo, L. (2012). Trans-synaptic teneurin signalling in neuromuscular synapse organization and target choice. Nature *484*, 237–241.

63. Goel, P., Dufour Bergeron, D., Böhme, M.A., Nunnelly, L., Lehmann, M., Buser, C., Walter, A.M., Sigrist, S.J., and Dickman, D. (2019). Homeostatic scaling of active zone scaffolds maintains global synaptic strength. J. Cell Biol. *218*, 1706–1724.

64. Vukoja, A., Rey, U., Petzoldt, A.G., Ott, C., Vollweiter, D., Quentin, C., Puchkov, D., Reynolds, E., Lehmann, M., Hohensee, S., et al. (2018). Presynaptic Biogenesis Requires Axonal Transport of Lysosome-Related Vesicles. Neuron *99*, 1216–1232.e7.

65. Pack-Chung, E., Kurshan, P.T., Dickman, D.K., and Schwarz, T.L. (2007). A Drosophila kinesin required for synaptic bouton formation and synaptic vesicle transport. Nat. Neurosci. *10*, 980–989.

66. Koles, K., Irvine, K.D., and Panin, V.M. (2004). Functional characterization of Drosophila sialyltransferase. J. Biol. Chem. *279*, 4346–4357.

67. Inaki, M., Yoshikawa, S., Thomas, J.B., Aburatani, H., and Nose, A. (2007). Wnt4 is a local repulsive cue that determines synaptic target specificity. Curr. Biol. *17*, 1574–1579.

68. McNeill, E.M., Thompson, C., Berke, B., Chou, V.T., Rusch, J., Duckworth, A., DeProto, J., Taylor, A., Gates, J., Gertler, F., et al. (2020). Drosophila enabled promotes synapse morphogenesis and regulates active zone form and function. Neural Dev. *15*, 4.

69. Blunk, A.D., Akbergenova, Y., Cho, R.W., Lee, J., Walldorf, U., Xu, K., Zhong, G., Zhuang, X., and Littleton, J.T. (2014). Postsynaptic actin regulates active zone spacing and glutamate receptor apposition at the Drosophila neuromuscular junction. Mol. Cell. Neurosci. *61*, 241–254.

70. Amos, L.A. (2008). The tektin family of microtubule-stabilizing proteins. Genome Biol. *9*, 229.

71. Norrander, J., Larsson, M., Ståhl, S., Höög, C., and Linck, R. (1998). Expression of ciliary tektins in brain and sensory development. J. Neurosci. *18*, 8912–8918.

72. Meltzer, H., Marom, E., Alyagor, I., Mayseless, O., Berkun, V., Segal-Gilboa, N., Unger, T., Luginbuhl, D., and Schuldiner, O. (2019). Tissue-specific (ts)CRISPR as an efficient strategy for in vivo screening in Drosophila. Nat. Commun. *10*, 2113.

73. Baccino-Calace, M., Schmidt, K., and Muller, M. (2022). The E3 ligase Thin controls homeostatic plasticity through neurotransmitter release repression. eLife *11*, e71437.

74. Blatow, M., Caputi, A., Burnashev, N., Monyer, H., and Rozov, A. (2003). Ca^{2+} buffer saturation underlies paired pulse facilitation in calbindin-D28k-containing terminals. Neuron *38*, 79–88.

75. Nakamura, Y., Harada, H., Kamasawa, N., Matsui, K., Rothman, J.S., Shigemoto, R., Silver, R.A., DiGregorio, D.A., and Takahashi, T. (2015). Nanoscale distribution of presynaptic Ca(2+) channels and its impact on vesicular release during development. Neuron *85*, 145–158.

76. Ghelani, T., and Sigrist, S.J. (2018). Coupling the structural and functional assembly of synaptic release sites. Front. Neuroanat. *12*, 81.

77. Jorquera, R.A., Huntwork-Rodriguez, S., Akbergenova, Y., Cho, R.W., and Littleton, J.T. (2012). Complexin controls spontaneous and evoked neurotransmitter release by regulating the timing and properties of synaptotagmin activity. J. Neurosci. *32*, 18234–18245.

78. Newman, Z.L., Bakshinskaya, D., Schultz, R., Kenny, S.J., Moon, S., Aghi, K., Stanley, C., Marnani, N., Li, R., Bleier, J., et al. (2022). Determinants of synapse diversity revealed by super-resolution quantal transmission and active zone imaging. Nat. Commun. *13*, 229.

79. Mrestani, A., Pauli, M., Kollmannsberger, P., Repp, F., Kittel, R.J., Eilers, J., Doose, S., Sauer, M., Sirén, A.L., Heckmann, M., et al. (2021). Active zone compaction correlates with presynaptic homeostatic potentiation. Cell Rep. *37*, 109770.

80. Scott, H., and Panin, V.M. (2014). N-glycosylation in regulation of the nervous system. Adv. Neurobiol. *9*, 367–394.

81. Kawabe, H., and Brose, N. (2011). The role of ubiquitylation in nerve cell development. Nat. Rev. Neurosci. *12*, 251–268.

82. Cho, R.W., Buhl, L.K., Volfson, D., Tran, A., Li, F., Akbergenova, Y., and Littleton, J.T. (2015). Phosphorylation of Complexin by PKA Regulates Activity-Dependent Spontaneous Neurotransmitter Release and Structural Synaptic Plasticity. Neuron *88*, 749–761.

83. Miśkiewicz, K., Jose, L.E., Bento-Abreu, A., Fislage, M., Taes, I., Kasprowicz, J., Swerts, J., Sigrist, S., Versées, W., Robberecht, W., et al. (2011). ELP3 controls active zone morphology by acetylating the ELKS family member Bruchpilot. Neuron *72*, 776–788.

84. DiAntonio, A., Haghighi, A.P., Portman, S.L., Lee, J.D., Amaranto, A.M., and Goodman, C.S. (2001). Ubiquitination-dependent mechanisms regulate synaptic growth and function. Nature *412*, 449–452.

85. Ednie, A.R., and Bennett, E.S. (2012). Modulation of voltage-gated ion channels by sialylation. Compr. Physiol. *2*, 1269–1301.

86. Kurmangaliyev, Y.Z., Yoo, J., Valdes-Aleman, J., Sanfilippo, P., and Zipursky, S.L. (2020). Transcriptional programs of circuit assembly in the drosophila visual system. Neuron *108*, 1045–1057.e6.

87. Paul, A., Crow, M., Raudales, R., He, M., Gillis, J., and Huang, Z.J. (2017). Transcriptional architecture of synaptic communication delineates GABAergic neuron identity. Cell *171*, 522–539.e20.

88. Huntwork, S., and Littleton, J.T. (2007). A complexin fusion clamp regulates spontaneous neurotransmitter release and synaptic growth. Nat. Neurosci. *10*, 1235–1237.

89. Marrus, S.B., Portman, S.L., Allen, M.J., Moffat, K.G., and DiAntonio, A. (2004). Differential localization of glutamate receptor subunits at the Drosophila neuromuscular junction. J. Neurosci. *24*, 1406–1415.

90. Hagel, K.R., Beriont, J., and Tessier, C.R. (2017). Drosophila Cbp53E regualtes axon growth at the neuromuscular junction. PLoS One *10*, e0132636.

91. Dobin, A., Davis, C.A., Schlesinger, F., Drenkow, J., Zaleski, C., Jha, S., Batut, P., Chaisson, M., and Gingeras, T.R. (2013). STAR: ultrafast universal RNA-seq aligner. Bioinformatics *29*, 15–21.

92. Li, B., and Dewey, C.N. (2011). RSEM: accurate transcript quantification from RNA-Seq data with or without a reference genome. BMC Bioinformatics *12*, 323.

Please cite this article in press as: Jetti et al., Molecular logic of synaptic diversity between *rosophila* tonic and phasic motoneurons, Neuron 2023), https://doi.org/10.1016/j.neuron.2023.07.019

STAR METHODS

KEY RESOURCES TABLE

REAGENT or RESOURCE	SOURCE	IDENTIFIER
Antibodies		
Anti-Brp (mouse)	Developmental Studies Hybridoma Bank	Cat nc82; RRID: AB_2314867
Anti-elav (rat)	Developmental Studies Hybridoma Bank	Cat Elav-9F8A9
Anti-GFP (rabbit)	Thermo Fisher Scientific	Cat A21311; RRID: AB_221477
rabbit anti-Cpx (rabbit)	Published in Huntwork and Littleton[88]	N/A
anti GluRIIB (rabbit)	Published in Marrus et al.[89]	N/A
Goat anti-Mouse IgG (H+L) Alexa 488	Thermo Fisher Scientific	Cat A32723; RRID: AB_2633275
GFP Polyclonal Antibody, Alexa Fluor 488	Thermo Fisher Scientific	Cat A21311; RRID: AB_221477
Goat anti-rabbit, Alexa Fluor 488	Thermo Fisher Scientific	Cat A11008; RRID: AB_143165
Goat anti-Mouse IgG (H+L) Alexa Fluor Plus 555	Thermo Fisher Scientific	Cat A32727; RRID: AB_ 2633276
Goat anti-Rat IgG (H+L) Alexa Fluor 647	Thermo Fisher Scientific	Cat A-21247 RRID: AB_141778
Goat anti-Mouse IgG Atto 488	Sigma	Cat 62197-1ML-F
Goat anti-Rabbit-IgG - Atto 550 antibody	Sigma	Cat 43328-1ML-F
Goat anti-Rabbit IgG - Atto 488 antibody	Sigma	Cat 18772-1ML-F
Goat anti-Mouse IgG−Atto 550 antibody	Sigma	Cat 43394-1ML-F
alexa fluor 555 goat anti rat	Thermo Fisher Scientific	Cat A-21434
Anti-HRP, Cy3 (goat)	Jackson ImmunoResearch Laboratories	Cat 123-165-021; RRID: AB_2338959
Chemicals, peptides, and recombinant proteins		
Sylgard 184 (polydimethylsiloxane, PDMS)	Dow Corning	Cat 184Kit
All-trans retinal	Sigma	Cat 116-31-4
Vectashield mounting medium	Vector Laboratories	Cat H-1000, RRID: AB_2336789
ProLong™ Diamond Antifade Mountant	Thermo Fisher Scientific	Cat P36970
Normal Goat Serum	Invitrogen	Cat 16210064
RNaseZap™ RNase Decontamination Solution	Thermofisher scientific	Cat AM9780
RNaseOUT™ Recombinant Ribonuclease Inhibitor	Thermofisher scientific	Cat 10777-019
Protease Type XIV (Protease from Streptomyces griseus)	sigma	Cat P5147-1G
Hard-Shell® 384-Well PCR Plates, thin wall, skirted, clear/clear	Bio-rad	Cat HSP3801
Experimental models: Organisms/strains		
Wild Type (w1118)	Bloomington Drosophila Stock Center (BDSC)	RRID: BDSC_3605
w[1118]; P{y[+t7.7] w[+mC]=GMR94G06-GAL4}attP2	BDSC	RRID: BDSC_40701
w[1118]; P{y[+t7.7] w[+mC]=GMR27E09-GAL4}attP2	BDSC	RRID: BDSC_49227
P{w[+mW.hs]=GawB}OK6	BDSC	RRID: BDSC_ 64199
w[*]; P{y[+t7.7] w[+mC]=10XUAS-IVS-mCD8::GFP}attP2	BDSC	RRID: BDSC_32185
y[1] w[*] Mi{y[+mDint2]=MIC}DIP-alpha [MI02031]	BDSC	RRID: BDSC_34458

(*Continued on next page*)

Please cite this article in press as: Jetti et al., Molecular logic of synaptic diversity between *rosophila* tonic and phasic motoneurons, Neuron 2023), https://doi.org/10.1016/j.neuron.2023.07.019

ontinued

REAGENT or RESOURCE	SOURCE	IDENTIFIER
y[1] w[*]; Mi{y[+mDint2]=MIC}Toll-6 [MI02127]/TM3, Sb[1] Ser[1]	BDSC	RRID: BDSC_34467
P{KK101895}VIE-260B	VDRC	VDRC: BDSC_ 105137
Toll-6^{ex13}	BDSC	RRID: BDSC_64072
Myd^{3PM71}	Published in Sidisky et al.[58]	PMID: 33667157
y[1] w[1118]; PBac{y[+mDint2] w[+mC]= UAS-ChR2.T159C}VK00018	BDSC	RRID: BDSC_58373
UAS BRP-GCaMP7s	N/A	this study
y[1] w[*]; Mi{Trojan-GAL4.2}Wnt4 [MI03717-TG4.2]	BDSC	RRID: BDSC_67449
y[1] w[*]; Mi{Trojan GAL4.2}myd [MI08258-TG4.2]	BDSC	RRID: BDSC_76695
w*; Mi{Trojan-GAL4.1}DIP-η$^{MI07948-TG4.1}$/ CyO; TM2/TM6B, Tb^{1}	BDCS	RRID: BDSC_ 90318
y[1] w[*]; Mi{GT-GAL4}DIP-gamma [MI03222-GAL4]/TM3, Sb[1]	BDSC	RRID: BDSC_90315
y[1] v[1]; P{y[+t7.7] v[+t1.8] =TRiP.HMJ30037}attP40	BDSC	RRID: BDSC_ 62960
y^{1} sc* v^{1} sev^{21}; P{TRiP.HMS02344}attP2	BDSC	RRID: BDSC_41947
w^{1118}; Mi{ET1}CG15537^{MB10928}	BDSC	RRID: BDSC_29170
P{KK106520}VIE-260B	VDRC	RRID: VDRC_108326
y[1] w[*]; Mi{y[+mDint2]=MIC}Unc-115b [MI04996] p24-2[MI04996]	BDSC	RRID: BDSC_37998
P{w[+mC]=ana[+m]}1, w[*]; P{ry[+t7.2] =A92}ana[1]	BDSC	RRID: BDSC_ 8927
y^{1} w*; Mi{MIC}kibra^{MI09242}/TM3, Sb^{1} Ser^{1}	BDSC	RRID: BDSC_ 51266
Mi{MIC}CG31323[MI10440]	BDSC	RRID: BDSC_ 51266
Cbp53E^{Mi22} mutant	Published in Hagel et al.[90]	PMID: 26167908
SiAT ^{L22} mutant	Published in Repnikova et al.[52]	PMID: 20445073
Wnt4^{C1}	BDSC	RRID: BDSC_6651
w* P{EP}ben^{G963}	BDSC	RRID: BDSC_33464
w*; Skp2^{ex9}	BDSC	RRID: BDSC_59000
y^{1} v^{1}; P{TRiP.HMJ23893}attP40	BDSC	RRID: BDSC_62439
y^{1} w*; Mi{MIC}Roc2^{MI09751}	BDSC	RRID: BDSC_53164
y^{1} w*; P{EP}hpo^{G3315}	BDSC	RRID: BDSC_ 27105
y^{1} w*; P{EP}Ube4B^{G13471}	BDSC	RRID: BDSC_28402
y^{1} sc* v^{1} sev^{21}; P{TRiP.HMS00838}attP2	BDSC	RRID: BDSC_33898
y^{1} w* Mi{MIC}CG43737^{MI10158}	BDSC	RRID: BDSC_53823
Software and algorithms		
Clampex	Molecular Devices	Version: 10.4
Zen software	Carl Zeiss	N/A
MATLAB	MathWorks	Versions: R2017b, R2018a, R2019a, R2020a, R2021a
R	R-Studio	N/A
Prism	Graphpad software	RRID:SCR_002798; v8.3.0 https://www.graphpad.com/scientific-software/prism/
Python	N/A	N/A
Graphpad PRISM	Graphpad	RRID: SCR_002798
Volocity software	PerkinElmer	https://www.volocity4d.com/

(*Continued on next page*)

Please cite this article in press as: Jetti et al., Molecular logic of synaptic diversity between *rosophila* tonic and phasic motoneurons, Neuron 2023), https://doi.org/10.1016/j.neuron.2023.07.019

ontinued

REAGENT or RESOURCE	SOURCE	IDENTIFIER
LAS X LS software	Leica	https://www.leica-microsystems.com/products/microscope-software/p/leica-las-x-ls/
Huygens Software	Scientific Volume Imaging	https://svi.nl/Huygens-Software
Image J/Fiji	N/A	https://imagej.net/software/fiji/downloads
Abode Illustrator	Abode	RRID: SCR_010279
Deposited data		
Isoform-Patch-seq sequencing reads and processed gene expression counts including raw RNA-Seq fastq files, gene-level integer count data and l2tpm, and isoform-level integer count data and l2tpm	This paper	GEO: GSE222976

RESOURCE AVAILABILITY

Lead contact

Further information and requests for resources and reagents should be directed to and will be fulfilled by the lead contact, Dr. J. Troy Littleton (troy@mit.edu).

Materials availability

All unique/stable reagents generated in this study are available from the lead contact without restriction.

Data and code availability

All Isoform-Patch-seq RNA profiling raw data is available at NCBI under the GEO accession GSE222976.
This study did not generate new code.
Any additional information required to reanalyze data reported in this paper is available from the lead contact upon request.

EXPERIMENTAL MODEL AND STUDY PARTICIPANT DETAILS

Drosophila stocks

Fly stocks were raised at 25°C on standard molasses food in an incubator with 12 h day/night cycle. Actively crawling third-instar larvae that were size and age matched were used for all experiments. Both male and female third-instar larvae were used to carry out experimental procedures unless indicated. The experimenters were not blinded to genotype. w^{1118} or $OK6^{Gal4}$ driver lines were used as control as indicated. Genotypes of the flies used were reported in the figure legend. All strains used in the study are indicated in the key resources table. No vertebrate animals were used in this study, so institutional permission and oversight, health/immune status, participants involvement in prior procedures, and drug or naïve state, is not applicable.

METHOD DETAILS

Larval fillet preparation

Wandering third-instar larva were dissected in cold Ca^{2+} free hemolymph-like-3 (HL3) saline solution consisting of the following in (mM): 70 NaCl, 5 KCl, 10 NaHCO3, 10 MgCl2, 115 sucrose, 4.2 trehalose, and 5 HEPES (pH 7.2). Evoked synaptic potentials (EJPs) were recorded from muscle 1 using a modified fillet preparation. Third-instar larvae were pinned down in a sylgard plate and a lateral cut was made from the anterior to the posterior end. CNS, gut, and fat bodies were gently removed. After the dissection, saline was replaced with HL3 containing 0.5 mM calcium prior to electrophysiology.

Optogenetic stimulation

To stimulate Is or Ib MN NMJs, $UAS^{ChR2\text{-}T159C}$ was expressed using Is- or Ib-Gal4 drivers. Third-instar larvae were grown in standard fly food supplemented with 0.5 mM all-trans-retinal. To prevent photoconversion of all-trans-retinal, aluminum foil was wrapped around food vials and larva were then grown under standard conditions as described. Optogenetic stimulation of Ib or Is MN terminals was carried out using a CoolLED pE-4000 system to deliver short blue light pulses (470 nm). Light pulses were applied via a 10X Olympus water objective for a duration of 50 to 100 μs with an interval 5 s to elicit unitary synaptic potentials in a reliable manner.

Please cite this article in press as: Jetti et al., Molecular logic of synaptic diversity between *rosophila* tonic and phasic motoneurons, Neuron 2023), https://doi.org/10.1016/j.neuron.2023.07.019

Sharp electrode current-clamp electrophysiology

Sharp electrodes were backfilled with 3M KCl using gel loading tips. The resistance of the sharp electrodes was in the range of 20 to 30 mOhm after filling with 3M KCl. Optically evoked synaptic potentials were measured in current-clamp mode using a Multiclamp 700b amplifier (Axon instruments), digitized with Digidata 1440 (Axon instruments), and sampled with pClamp10 software. Signals were acquired at 10 kHz and low pass filtered at 2 kHz. Synaptic potentials were recorded from muscle 1 NMJs in abdominal segments 3 and 4. Resting Vm and muscle input resistance were monitored at the beginning and end of each recording. Recordings were excluded if resting Vm and muscle input resistance (Rin) changed by more than 20%.

Two-electrode voltage clamp electrophysiology

Excitatory junctional currents (EJCs) were recorded from third-instar larvae at muscle 4 using two-electrode voltage clamp (TEVC) at −70 mV holding potential in HL3.1 saline (in mM, 70 NaCl, 5 KCl, 10 NaHCO3, 10 MgCl2, 5 trehalose, 115 sucrose, 5 HEPES, pH 7.2). Recordings were made from muscles with an initial *Vm* in the range of −50 mV to −70 mV using intracellular borosilicate glass electrodes with resistances of 15–20 MΩ, filled with 3 M KCl. Fire-polished suction electrodes with tip openings of 5-8 μm were used to stimulate axons using a Master-8 (A.M.P.I.). Third-instar larvae were dissected in ice-cold Ca^{2+}-free HL-3 saline, and the fillet preparation was replaced with HL-3 containing 1 mm Ca^{2+} prior to the recordings. Recorded signals were amplified using AxoClamp-2B amplifier, digitized using Digidata 1440A, and synaptic currents recorded using pClamp 9.1 software (Molecular Devices, Sunnyvale, CA). Paired pulse experiments were carried out with 25, 50, and 75ms interstimulus intervals, and 20 sweeps were averaged to obtain average 1st and 2nd EJC amplitudes. Paired-pulse ratio was calculated by dividing the 2nd EJC amplitudes by 1st EJC amplitudes.

Isoform-Patch-seq protocol

To prevent contamination of Patch-seq samples, the fly station, lab bench, dissection microscopes, patch-clamp rig, perfusion apparatus, and microelectrode laser puller were cleaned with 70% ethanol, followed by RNase zap. Borosilicate microcapillaries, glassware, milli-Q water and other supplies were autoclaved to avoid contamination. Single Ib and Is MN or muscle 1 or 4 samples were collected using patch electrodes pulled using autoclaved borosilicate microcapillaries. Third-instar larval fillets were dissected in ice-cold sterile external saline consisting of (in mM): 103 NaCl, 3 KCl, 5 TES, 8 trehalose, 10 glucose, 26 NaHCO3, 1 NaH2PO4, 4 MgCl2. The osmolarity of the sterile external saline was adjusted to 275-280 mOsm. The sterile saline was bubbled with carbogen gas (95% O2 and 5% CO2) and adjusted to pH 7.3. During Patch-seq sample collection, sterile external saline was continuously superfues over the CNS of intact third-instar larvae at a flow rate of 2-3 ml per minute. Following sample collection, 70% ethanol was run through the custom-made perfusion system to maintain sterile conditions and avoid contamination.

To gently disrupt the glia sheath surrounding Ib and Is MNs, 0.5 to 1% protease (Type XIV, Streptomyces griseus, Sigma) was applied using a whole-cell electrode (2 to 3 μm tip size). Glial sheath disruption was carefully observed using microscope optics, followed by protease treatment. After glia sheath disruption, residual protease was quickly washed out by increasing the flow rate of external saline to 5-7 ml per minute for 5-10 min, and the flow rate was returned back to 2-3 ml per minute for the remaining sample collection. Residual debris and glial sheath covering MNs were removed using a cleaning electrode (3 to 4 μm tip size) filled with external sterile saline to ensure a clean surface before MN samples were collected.

For Patch-seq collection, sterile whole-cell electrodes were filled with 1 μl of nuclease-free water containing 20 units/ul of RNAse inhibitor. To visualize the cell bodies of Is and Ib, MNs were genetically labeled using R94G06-Gal4 or R27E09-Gal4 expression of 10XUAS-IVS-mCD8::GFP. MN cell bodies were visualized using a BX51W Olympus microscope with a 40X water objective. Whole-cell electrodes were targeted to the MN cell bodies by applying continuous positive pressure using mouth suction. Somatic and nuclear contents of single MNs were gently collected into the electrode. After sucking up the somatic and nuclear content of single MNs, the electrode holder was carefully removed from the micromanipulator, and the tip of the electrode was broken gently into a 384 microwell in a quadrant pattern. Samples were collected from thoracic (T1-T3) and abdominal segments (A1-A8) from both sexes. To prevent temperature fluctuations, 384 microwell plates were maintained on dry ice in closed thermal coal. MN and muscle samples were collected into a 384 microwell plate in a quadrant fashion, and 96 samples were collected into one plate for library preparation. As a control, 2 or 3 wells were filled with nuclease-free water only. Samples were collected within a time window of 4 to 6 days and stored in a -80 freezer between sample collection. As larval single MN Patch-seq was not carried out previously, a pilot RNAseq analysis was performed to determine whether it was feasible to detect RNA profiles from single Ib and Is MNs. The pilot analysis robustly detected gene expression profiles in Is and Ib MNs. Samples from muscle 1 or 4 were collected using low resistance patch electrodes (tip size of 5 to 10 μm) filled with external saline and flash frozen on dry ice together with the MN samples in 384 well plates.

Single-cell RNA library preparation and sequencing

RNAseq libraries from single cells were prepared using a modified version of the SMART-seq2 single-cell protocol.[44] RNA from single cells was placed in Hard-Shell 384-well plates (Catalog HSP3801) in minimal volume (<2 uL). cDNA was prepared following a standard protocol using 1/3 recommended volumes for all reagents utilizing a Mosquito HV automated liquid handler (SPT Labtech). Amplified cDNA was purified using 0.75X SPRI beads, quantified using picogreen and spot-checked on a Fragment Analyzer (Agilent). Dual indexed Illumina libraries were prepared from cDNA using a reduced volume NexteraXT reaction (1:12) on the Mosquito HV. Final libraries were quantified using picogreen and spot-checked on a Fragment Analyzer before pooling and final

Please cite this article in press as: Jetti et al., Molecular logic of synaptic diversity between *rosophila* tonic and phasic motoneurons, Neuron 2023), https://doi.org/10.1016/j.neuron.2023.07.019

quantification using qPCR on a Roche LC480II. Libraries were run on an Illumina HiSeq2000 (single end 40nt) or Illumina NextSeq500 (paired-end 75nt).

Real-time PCR quantification of CG9003 RNAi knockdown

To quantify the efficacy of CG9003 RNAi knockdown, pan-cellular Tubulin-Gal4 (BL 5138) was crossed to UAS-CG9003 RNAi (BL 62439) at 25°C. Adult progeny were selected from multiple vials and placed in 1.5 mL tubes and frozen in liquid nitrogen, followed by a brief vortex to isolate heads, which were used as material for qPCR. For each genotype, three biological replicates were created using 40 heads per replicate. RNA was extracted (RNAeasy Plus Mini Kit, Qiagen, cat 74134), transcribed into a cDNA library (High Capacity cDNA Reverse Transcription Kit, Applied Biosystems, cat 4368814) and three technical replicates of each biological replicate were loaded onto a qPCR plate with SYBR Green (SsoAdvanced Universal SYBR Green Supermix, Biorad, cat 1725271). Primers against CG9003

(5'- TGGCTGTCCAAATCTCATGG, 5'- GCCAGGCACATTATGGCATT)were designed to bridge an intron to amplify only mRNA. Primers against Actin5C were used as control:

(5'- CGAAGAAGTTGCTGCTCTGGTTGT, 5'- GGACGTCCCACAATCGATGGGAAG). qPCR was run on a Biorad CFX Connect at an annealing temperature of 62°C. To calculate Cq values, biological and technical replicates were averaged and CG9003 fluorescence was normalized using Actin with the following methodology: Cq = CG9003 – Actin, and Cq = Cq CG9003 - Cq control fly line. Linear value (2^- Cq) quantification demonstated that a 83% and 64% reduction in CG9003 RNA in progeny compared to RNAi and Gal4 controls, respectively.

Synaptic GCaMP imaging

Third-instar larvae were dissected in Ca^{2+} free HL3. Optical quantal imaging experiments were carried out using HL3.1 containing 20 mm Mg^{2+} and 1.3 mm Ca^{2+} using a confocal microscope (Perkin Elmer) with a spinning-disk confocal head (CSU-X1; Yokogawa), ImagEM X2 EM-CCD camera (Hamamatsu), and 488, 565, and 670 lasers. An Olympus LUMFL N 60X objective with a 1.10 NA was used to acquire GCaMP7s signals from muscle 4 NMJs. To identify individual AZs, a CRISPR Cac-TagRFP[37] strain that endogenously tags the Cac protein was used and membrane tagged (myristoylated) GCaMP7s was expressed in muscles using a Mef2-LexA driver. Prior to quantal imaging, 3D image stacks of muscle 4 NMJs were collected to identify the spatial location of individual AZs denoted by localized Cac-TagRFP fluorescence. To measure evoked release probability of Ib and Is MNs, axons were stimulated using minimal stimulation protocols. Care was taken to recruit both Is and Ib by adjusting the stimulation intensity during imaging experiments. Stimulation was applied using an AMPI Master-8 stimulator at 0.3 Hz frequency for a duration of 200 μs for an experimental time window of 5 min. Volocity 3D Image Analysis software (PerkinElmer) was used to acquire and analyze data.

Immunohistochemistry of NMJ and CNS samples

Larval fillets were dissected in ice-cold Ca^{2+} free HL-3 solution as described earlier. The fillet's CNS was kept intact to validate expression patterns of DEGs at MN somas and NMJs. Larval fillet samples were fixed in 4% formaldehyde for 15-20 min at room temperature, washed in PBST (PBS with 0.3% Triton X-100) for 1 h at room temperature, and incubated in blocking buffer (PBST+ 5% normal goat serum) for 1 h at room temperature on a shaker. All primary and secondary antibodies were diluted in PBT. Samples were incubated in the primary antibody at 4°C overnight while rocking, with three 20 min washes of PBT at room temperature before secondary antibody incubation. Fillet samples without the CNS were incubated in secondary antibody for 2 h, whereas CNS intact fillet samples were incubated in secondary overnight at 4°C while rocking. Samples were mounted in Vectashield and imaged with a Zeiss confocal microscope using a 60x (NA = 1.3) oil objective. Samples for STED imaging were mounted in prolong diamond mount to improve quality of STED depletion. Primary and secondary antibodies used in this study are listed in the key resources table.

Confocal imaging, image acquisition and processing

A Zeiss LSM 780 laser-scanning confocal microscope (Carl Zeiss) with a 63x/1.3NM oil-immersion objective (Carl Zeiss) was used for data collection for bouton and AZ quantification. Confocal z stacks were obtained in 1 mm intervals at a resolution of 1084x1084. Images were processed with Zen software (Zeiss) to obtain maximum projections. Photoshop (Adobe) or Fiji were used for image rotation and cropping. Adobe Illustrator was used to assemble images and prepare figures.

STED imaging

Dual or triple channel STED imaging of Ib and Is AZs was carried out using a Leica SP8 confocal/STED 3 microscope (Leica Microsystems, Mannheim, Germany) with 100X, 1.44 NA oil objective and immersion oil (Leica Type F, refractive index 1.5180). For STED, immunohistochemistry protocols were modified to improve nanoscale analysis of AZs. Instead of 20 min of 4% PFA fixation, 10 min of fixation were used following calibration experiments. After overnight primary antibody incubation, samples were washed 3-4 times in PBST for 1 h and incubated in Atto-conjugated secondary 488 antibodies, Alexa 555 and Hrp 647. Samples were washed three times for 1 h in PBST and mounted on slides using prolong diamond mount.

Triple or dual-color sequential STED scans were acquired using the STED microscope with gated detectors and 40 nm x-y resolution. Based on pilot studies, a combination of Atto 488 and Alexa Fluor 565 were selected as optimal for analyzing nanoscale AZ

Please cite this article in press as: Jetti et al., Molecular logic of synaptic diversity between *rosophila* tonic and phasic motoneurons, Neuron 2023), https://doi.org/10.1016/j.neuron.2023.07.019

organization as the two dyes were photostable and showed no shifts in excitation of wavelengths, and photobleaching of signals was significantly reduced compared to other tested dye combinations. Images were scanned at a pixel density of 1024 X 1024 (9 nm/pixel). Hrp 647, Alexa Fluor 555, and Atto 488 were excited with 633 nm, 555 nm, and 488 nm white light lasers, respectively, in the same sequential order at 2-5% 1.5 mW laser power. We depleted Atto 488 and Alexa Fluor 565 signals using 592 nm (75% of maximum power) and 660 nm (25% of maximum power) time-gated depletion lasers. During STED scanning, line accumulation of four times and frame averaging of three times was used. Eight times zoom was used to compare the nanoscale organization of AZs and other key synaptic proteins.

TEM sample preparation and imaging

TEM sample preparation was carried out on third-instar larval preparations from w^{1118} controls that were dissected in Ca^{2+}-free HL3.1 solution and fixed in freshly prepared fixative containing 1% glutaraldehyde, 4% formaldehyde, and 0.1 m sodium cacodylate for 10 min at room temperature. Fixed samples were microwaved in a BioWave Pro Pelco (Ted Pella, Inc, Redding, CA, USA) in the following order: (1) 100W 1 min, (2) 1 min off, (3) 100W 1 min, (4) 300W 20 s, (5) 20 s off, (6) 300W 20 s, with steps 4-6 repeated twice. Following microwaved steps, samples were incubated for 30 min at room temperature in fixative. Samples were washed in 0.1 M sodium cacodylate and 0.1 M sucrose and were stained for 30 min in 1% osmium tetroxide and 1.5% potassium ferrocyanide in 0.1 M sodium cacodylate solution. Samples were washed in 0.1 M sodium cacodylate and stained for 30 mins in 2% uranyl acetate. Samples were then embedded in epoxy resin (Embed 812; Electron Microscopy Sciences) and dehydrated through a graded series of ethanol and acetone. 50–60 nm range thin sections were collected on Formvar/carbon-coated copper slot grids and contrasted using lead citrate. A Tecnai G2 electron microscope (FEI, Hillsboro, OR, USA) equipped with a charge-coupled device camera (Advanced Microscopy Techniques, Woburn, MA, USA) was used to carry out TEM at 49,000 magnification at 80 kV. Ib and Is boutons at muscle 6/7 NMJs were analyzed to compare Ib and Is synaptic features. Ib and Is innervation were identified by their position on muscle 6/7 and associated SSR size. Only micrographs with bouton diameters larger than 2 μm were included in analysis for 1b boutons. For SV counting, T-bars at Ib and Is boutons were identified and Photoshop was used to draw concentric circles with 100 nm and 200 nm radii with the T-bar at the center. To quantify vesicle density, Volocity software was used to measure the area of the bouton and quantify the total number of SVs within it.

Data exclusion criteria

For synaptic GCaMP imaging experiments, data was excluded if larvae underwent significant muscle contractions. For electrophysiology experiments, data was excluded based on resting Vm (if resting Vm is above -60 vm) and input resistance threshold. In some cases, data with a sudden drop in resting Vm and Rin were also excluded from the analysis, as were samples where less than 20 traces were obtained during the recording. Patch-seq samples were excluded with low read number when less than 3000 genes were detected based on alignment to the *Drosophila* genome.

Replication of results

All experiments were carried out in at least three biological replicates, and all crosses were set up at least twice to obtain reproducible results from replicate to replicate. STED imaging was repeated several times to test variables such as duration of PFA fixation, mounting conditions, intensities for depletion laser, and concentrations of immunostaining reagents to exclude the possibility that differential nanoscale organization of Ib and Is AZs was due to any specific imaging condition. Differences Ib and Is nanoscale organization was highly reproducible in all biological replicates.

QUANTIFICATION AND STATISTICAL ANALYSIS

Electrophysiology data analysis

All electrophysiological recordings were analyzed using clampex software and custom-written MATLAB codes. To calculate the average amplitude of evoked EJPs, at least 20 evoked traces were acquired at 0.2 Hz and the average amplitude was determined using Clampex software. To exclude the possibility that optogenetically evoked response were graded responses, simultaneous electric and optogenetic stimulation were alternated, and pharmacology was used to confirm optogenetic responses were absent following action potential blockage.

Synaptic GCaMP imaging data analysis

Synaptic GCaMP imaging was analyzed using the Volocity 3D Image Analysis software (PerkinElmer). Prior to the analysis, a motion-correction algorithm was implemented to correct moment along X and Y directions. To robustly detect myrGCaMP7 synaptic signals, background subtraction was carried out using a composite stack of 5-6 images that lacked synaptic signals. Cac-TagRFP puncta position was used to detect AZ position using the 'find spot' algorithm in the Volocity software. Region of interests (ROIs) were automatically detected using this approach and ROIs were assigned to each Cac-TagRFP puncta for quantification of synaptic GCaMP events. MyrGCaMP7s flashes were assigned to ROIs by proximity. Only events occurring within 0.8 μM distance from ROI centers were analyzed. The time and XY coordinates of synaptic events were imported into Microsoft Excel to generate P_r maps. To calculate AZ P_r, the number of synaptic GCaMP events was divided by the number of electric pulses applied. High and low P_r AZs were color

Please cite this article in press as: Jetti et al., Molecular logic of synaptic diversity between *rosophila* tonic and phasic motoneurons, Neuron 2023), https://doi.org/10.1016/j.neuron.2023.07.019

coded in warm or cool colors, respectively. Experiments with a significant amount of image movement were not included in the analysis.

STED image analysis

All STED images were deconvolved using the deconvolution module in the Huygens software by applying the classical maximum likelihood estimation (CMLE) deconvolution algorithm to increase signal-to-noise. As Huygens software uses a signal reassignment-based deconvolution algorithm, it is feasible to carry out intensity measurements and comparisons between samples that were collected under the same imaging conditions. Deconvolved images were analyzed in ImageJ (Fiji) software to calculate the area of Is and Ib AZs. To determine the geometric organization of Is and Ib AZs, Wayne Rasband's ImageJ circularity plugin was used, where circularity is measured as *circularity = 4pi area/perimeter^2)*. If the CI index is 1, AZs are perfectly circular, and if CI index is 0 or close to 0, AZs are non-circular. CI index analysis robustly classified the geometric organization of Ib and Is AZs. ROIs were manually drawn around AZs to calculate area, perimeter, circularity index. To show differences in nanoscopic organization of AZs, intensity profile analysis, a complementary approach to CI index analysis, was performed. Intensity profiles of Ib and Is AZs were are also different, supporting distinct Ib and Is AZ structure. AZs lacking a core and lateralized AZs were excluded from the analysis.

Dataset Processing and Single-Sample Gene Set Enrichment Analysis

Paired-end reads were aligned to the *Drosophila melanogaster* transcriptome derived from assembly BDGP6 with Ensembl annotation release 92 and STAR version 2.5.3a.[91] Gene expression was quantified with RSEM version 1.3.0[92] with the calc-pme option. Raw transcript per million (TPM) values were offset by +1 and transformed to log 2 space and hierarchical clustering was done with protein coding genes and manual examination of the results was used to exclude outlier cells from downstream analysis. Integer count data was prepared for genes and isoforms from the posterior mean counts results and the data were used as input for differential expression testing and Seurat-based analyses.

Differential gene expression analysis

Integer count values derived from RSEM processing were used as input to differential expression analysis with DESeq2 (version 1.24.0)[45] using normal log fold change shrinkage. Differentially expressed genes or isoforms were defined as those having an absolute $\log_2$ fold change ≥ 1 and an adjusted p value 0.05. Differential expression data was visualized using TIBCO Spotfire Analyst version 7.11.1.

Visualization and clustering of single-cell data

Integer count data was imported into Seurat (version 3.0.0) running under R version 3.6.0 with and dimensionality reduction plots were prepared with umap (version 0.2.2.0) using dims of 1:20. Additional R packages include cowplot (version 0.9.4), ggplot2 (version 3.1.1) and dplyr (version 0.8.0.1).

Gene ontology analysis

To determine if sets of related genes or genes with related functions were differentially regulated in 1b and 1s MNs, a list of all genes rank-ordered by RSEM statistic was uploaded to the STRING database (https://string-db.org/). The search tool for Functional Enrichment Analysis was used with the organism set to *Drosophila melanogaster* with a 5% false discovery rate.

RNAseq analysis, heatmaps, and violin plots

For visualization, Matlab was used to plot heatmaps and scatterplots. The Seaborn statistical data visualization package (https://seaborn.pydata.org/) was used to make combined violin plots and swarm plots of transcript level data, running in the Spyder 4.2.1 IDE using Python 3.7.

Statistics and sample sizes

Statistical analysis was done using Graphpad Prism and R-Studio. In all the figures, data was represented as mean ± SEM (standard error of the mean). Statistical significance was determined using one-way ANOVA followed by post hoc comparison using Tukey's test for multiple comparisons, while student t-test was used for comparison of two groups. In figure legends, significance levels are represented as follow: *p < 0.05, **p < 0.01, ***p < 0.001, ****p < 0.0001, ns not significant. Sample size was chosen based on standard sample size in the field for all the experiments except for isoform-Patch-seq analysis. Sample size for isoform-Patch-seq experiments was determined based on robustness of known marker gene detection for Ib and Is neurons. Details of the statistical analyses, statistical significance sample size, and what n represents were reported in each figure legend.